INSTABILITIES AROUND AN OSCILLATING CYLINDER AND EMPIRICAL STUDY OF INTERNAL WAVES

FARAH RASHID

Thesis for the Degree of Philosophiae Doctor

August, 2012

Department of Mathematics, Mechanics Division
University of Oslo, Pb. 1053 Blindern, No-0316
Norway

Series of dissertations submitted to the
Faculty of Mathematics and Natural Sciences, University of Oslo
No. 1311

ISSN 1501-7710

Cover: Inger Sandved Anfinsen.
Printed in Norway: AIT Oslo AS.

Produced in co-operation with Akademika publishing.
The thesis is produced by Akademika publishing merely in connection with the thesis defence. Kindly direct all inquiries regarding the thesis to the copyright holder or the unit which grants the doctorate.

"In the middle of difficulty lies opportunity."

Albert Einstein

Acknowledgements

First and foremost, I would like to thank my greatest teacher of all: God. I feel that I am able to share my work with the world for a reason. I can and will never forget what a fortune I have had in just being here, and that it came with a lesson, learning and responsibility.

I offer my sincerest gratitude to my supervisor, Karsten Trulsen, who has supported me throughout my thesis with his patience and knowledge whilst allowing me the room to work in my own way. I attribute the level of my work to his encouragement and effort and without him this thesis, too, would not have been completed. One simply could not wish for a better and friendlier supervisor. I would also like to thank Atle Jensen and Arnaud Sanchis for their cooperation and constructive feed back. I am grateful to John Grue for his sharing of knowledge. In the Hydrodynamics lab, I was aided by Svein Vesterby in running the experiment; who being a very fine technician always came up with a solution whenever required. I would like to thank the department administration for their support which made it possible for me to complete this work.

Furhermore I would like to express my gratitude to my colleagues at UiO. In particular, Karina B. Hjelmervik and Jostein Kolaas for good cooperation and support, and also Odin Gramstad, Huiming Zeng, Birgit Kjoss Lynge, Qiao Jie Yang, Erika Kristina Lindstrøm, Anis Ayati, Magnus Vartdal, Arne Bøckmann, Daniela Laskovski, Stig Grafsrønningen and everyone for their support and discussions. I was lucky to have a friendly and cheerful Erika around, she provided something much greater in all the years I've known her.

I am thankful to Durranis, Mohammad Razzaq, Shamim Razzaq and Afzal Bhai for their help and support during my stay here. In particular, I would like to thank Shamim Razzaq for being with me and my girls at the hard times.

I am thankful to my father who has always encouraged me for higher studies and for his confidence in me. I am thankful to Arshad Bhai, Mani Bhai, Khola and Amir Sultan for their support and prayers. I feel very lucky and blessed for having Hina with me throughout this journey. Special gratitude goes to my dearest Hina Aftab and my big sister Tahira, words cannot express what your support, love, stability and patience mean to me. Finally, my very special thanks to my two kids Rumaisa and Maneha for sharing their childhood wisdom and earnest joy of life. Thankyou for being a loving family.

This work is dedicated to my late Mother *(Inna lilla he wa ina ilehe rajeoon)* with Love.

Preface

"Be careful what you water your dreams with.
Water them with worry and fear
and you will produce weeds
that choke the life from your dream.
Water them with optimism and solutions
and you will cultivate success.
Always be on the lookout for ways
to turn a problem
into an opportunity for success.
Always be on the lookout
for ways to nurture your dream."

Lao Tzu

Contents

INTRODUCTION

Introduction

1 Motivation

Water is the most abundant compound on Earth's surface, covering about 70 percent of the planet. Wave motion in water is one of the most striking observable phenomena in nature. Waves cannot exist by themselves for they are caused by some form of disturbance. Interestingly, an object's oscillation in still water can generate wave motion. Wind waves or, more precisely, wind-generated waves are surface waves that occur on the free surface of oceans, seas, lakes, rivers, and canals or even on small puddles and ponds. They result from the wind blowing over a stretch of fluid surface. A stably-stratified ocean supports internal gravity waves. Internal waves, which occur within the subsurface layers of the ocean where density stratification is strong, are generated when the interface between the layers is disturbed. Disturbances are often caused by tidal flow passing over shallow underwater obstacles such as a sill or a shallow ridge.

Wave body interaction has been studied for many practical reasons. These reasons include marine and offshore structures, which are used for a variety of functions and at various water depths and they are exposed to harsh marine environment, one such example is shown in figure 1. Some of their significant design considerations are loads caused by wind and waves, and motion of the platform. In this regard sinusoidally oscillating flow past a fixed cylinder has acquired a lot of attention from fluid dynamicists and engineers because of its theoretical and practical significance. Stokes (1851) was the first to find the force acting on a cylinder or a sphere oscillating sinusoidally in a viscous fluid. In his remarkable study he described analytically the associated components of the force involving velocity and acceleration respectively. Morison *et al.* (1950) did experimental and theoretical investigations about the force associated with the surface waves on a pile. Through their study they described this force to be consisting of two components i.e. the drag force and an inertia force. Keulegan & Carpenter (1958) investigated inertia and drag coefficients of cylinders in simple sinusoidal currents. They put forward the period parameter $\frac{U_m T}{D}$, called the Keulegan Carpenter number K. They studied the average values of inertia and drag coefficients that vary over a wave cycle and

Figure 1: Hywind turbine installed in the North Sea, Norway in 2010. Image source *http://en.wikipedia.org/wiki/File:Hywind.jpg*

described that these variations can be correlated by *K*. Wang & Chang (1968) extended Stokes (1851) analysis by inner and outer expansions of the drag coefficient and inertia coefficient.

Since then a great deal of work has been done, this includes experimental studies by Honji (1981), Hall (1984), Sarpkaya (1986), Otter (1990), Chaplin (2000), Johanning *et al.* (2001) and computational contributions by Lu *et al.* (1997) and Wu *et al.* (2007). Honji (1981) performed a very interesting experiment showing instabilities associated with the flow around a vertical cylinder oscillated back and forth in a fluid. These instabilities were later called Honji instabilities. Sarpkaya (1986) performed a series of experiments and hence confirmed Honjis work. He also confirmed the pioneering work of Stokes (1851) and Wang & Chang (1968) regarding drag coefficient. An *et al.* (2011) provided detailed computations and flow visualisations of Honji vortices below flow separation around a circular cylinder. In one of the very recent numerical studies by Suthon & Dalton (2012) about the observations on Honji instabilty, they investigated three-dimensional sinusoidally oscillating flow around an infinitely long cylinder to examine the onset of the Honji instability and to study the reasons that cause the Honji instability to rise. They also discussed the isosurfaces of circumferential vorticity pairing around the vertical cylinder which is shown in figure 2.

The investigation and calculation of the wave loads on vertical cylinders has gathered major attention of researchers and engineers, particularly over the last couple of decades

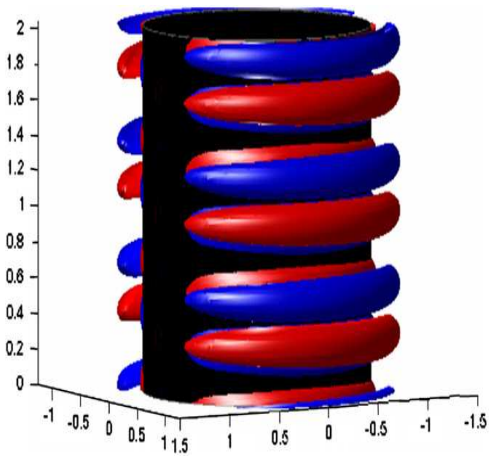

Figure 2: Isosurfaces of circumferential vorticity around a cylinder at the time of maximum mean velocity. (Suthon & Dalton, 2012)

as such studies are motivated by the need and requirement to build offshore structures in connection with oil and natural gas exploration and productions. Some of the offshore fixed platforms are shown in figure 3. Their installation may vary from deep water to shallow water along the bottom topography. There are also floating platforms and semi-submersible platforms. These offshore and marine structures experience environmental loading from the wind as well as they withstand other conditions, such as hydrodynamic loading from waves and sea currents. This includes both surface waves and internal waves. Osborne & Burch (1980) studied the internal waves in Andaman Sea and they observed that one drilling rig was spun through 90° and moved 100 feet by the passage of an internal solitory wave. Experimental study by Gavrilov & Ermanyuk (1996) described the forces exerted by internal waves on a stationary cylinder under stratification conditions with a large density gradient layer (pycnocline). They described a significant dependence of wave loads on pycnocline thickness.

Since the time internal waves were first reported by Nansen (1905), internal waves have gathered a great deal of considerations from researchers along with the increased number of under water activities. Researchers have studied and investigated various aspects of internal waves. Ekman (1904) carried out experimental and theoretical work about the internal wave propagation. Farmer & Smith (1980) and Apel *et al.* (1985) studied internal waves which were generated by tidal flows on release of large bodies of salt and fresh water, flowing from one part of ocean to the other. Wallace & Wilkinson (1988) and Helfrich (1992), in their experimental observations showed internal wave run-up on

slope and breaking of waves with the formation of boluses. Lamb (1994) numerically investigated nonlinear evolution of the internal wave field generated by tidal flow across a bank edge. They motivated their study by the complex internal wave phenomenon observed on Georges Bank. Experimental research by Grue *et al.* (1999) compared the experiments with a fully nonlinear interface model and weakly nonlinear Korteweg-de Vries (KdV) theory. Cai *et al.* (2003) investigated the forces and torques exerted by an internal soliton on cylindrical pile. In their study they employed Morison's method and introduced separation and regression analysis to estimate the forces on piles. They also recorded a set of observational data near Dongsha Islands in the northern South China Sea. Field studies done by Duda *et al.* (2004) and Ramp *et al.* (2004) recorded internal wave data at the continental slope in the Northern South China Sea. Their study was a combination of moored and ship board observations. They described in detail the internal waves as they propagated along the continental slope.

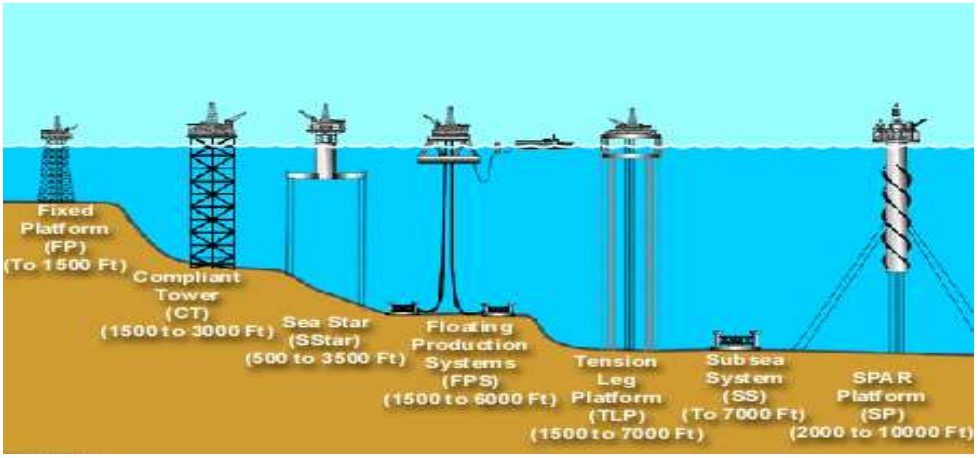

Figure 3: Schematic diagram of different types of platforms (Sadeghi, 2007)

Cai *et al.* (2005) extended their previous work of evaluating the forces exerted by internal solitons on cylindrical piles. In their study they put forward a method to estimate the force without observational current data using eigenfunction profile. In one of the recent computational study by Song *et al.* (2011), they established a numerical model for computing the action of internal solitory waves on marine structures and structure motion

responses by considering a cylindrical pile. They also compared the motion response of the platform under the action of internal soliton and surface waves.

The current thesis is comprised of three tasks. In the first section effort is made to numerically evaluate the hydrodynamic forces acting on a vertical oscillating cylinder. In this part of the study Honji instabilities have also been simulated numerically. The second section is based on experimental work. In the experimental studies the focus was to investigate the internal solitary waves behaviour over a flat bottom and sloping bottom respectively. Experiments with flat bottom were conducted to investigate shear-induced breaking of internal waves in stably stratified fluid system. In the third project an effort was made to record and investigate the internal wave behaviour and properties while propagating along the sloping bottom with linearly stratified fluid system.

1.1 Oscillating Vertical Cylinder

This section of study falls into a category of computations (Grue *et al.*, 2011). The fluid considered was viscous and waves were generated by oscillating a cylinder. Effort has been made to compute the flow and forces on a long vertical cylinder of diameter $D = 2R$ that oscillated in a fluid otherwise at rest. In this study Large Eddy Simulations (LES) and laminar flow computations were described by solving the plain or filtered Navier-Stokes equations.

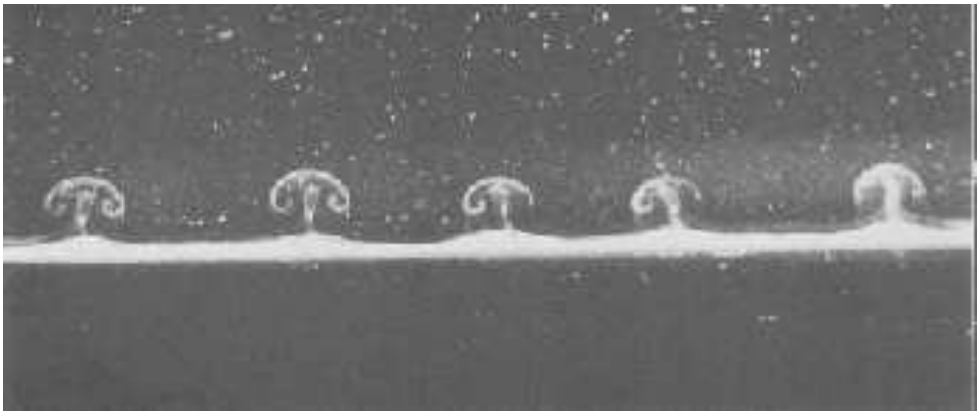

(a)

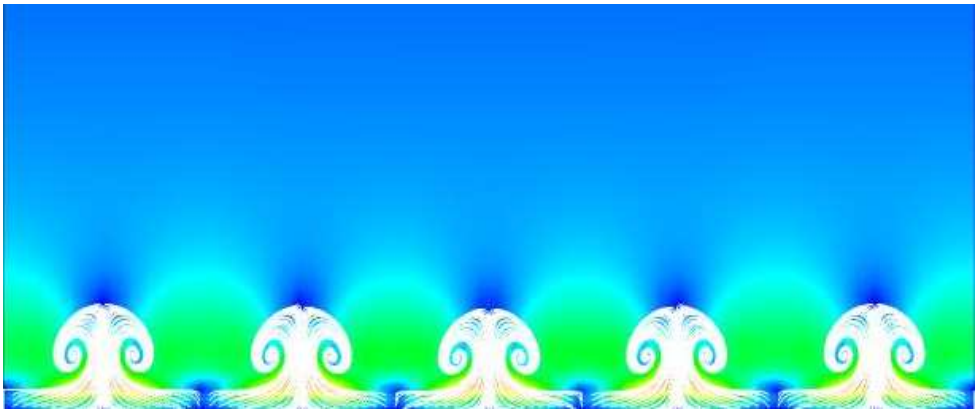

(b)

Figure 4: Upper frame (a) showing instabilities recorded in the lab by Honji (1981) and lower frame (b) the same instabilities numerically simulated by Grue *et al.* (2011)

The oscillatory flow was characterized by two parameters i.e. the Keulegan Carpenter number defined by $K = U_m T/D$ and the frequency parameter $\beta = D^2/\nu T = Re/K$, where the Reynolds number was given by $Re = U_m D/T$ (ν kinematic viscosity, T oscillation period, U_m maximal velocity).

The current calculations were performed for β in the range 197-61400 and K in the range of 0.5-4. The current calculations resolved the streak line patterns of the Honji instability that exemplify the local flow structures in the cylinder boundary layer. In the laminar range, secondary streaming was generated in the cylinder's boundary layer.

For sufficiently large oscillation amplitude and Keulegan Carpenter number, roll pattern became generated, superimposed on this streaming. The calculations compared well with the experimental measurements by Honji (1981). The experimental observation of Honji and numerically simulated Honji instabilities are shown in figure 2(a) and figure 2(b), respectively.

In the experiments performed by Honji (1981), he investigated the stability of the flow by oscillating a cylinder in water at rest. He described a three dimensional instability of the flow appearing in the form of an oscillatory cell pattern in the boundary layer of the oscillating cylinder. The behaviour of the cell exhibited locally a mushroom-like streak line pattern. Honji expressed the appearance of the instability in terms of the non-dimensional oscillation amplitude d_0/D and Stokes number $St = fD/\nu$ with $f = 1/T$ the frequency. Sarpkaya (1986) performed experiments with fixed cylinder in an oscillating water. He discussed that the presence of the Honji instability along the cylinder boundary caused a drag force that was higher than that predicted by Wang & Chang (1968). Otter (1990) described the damping forces close to the Wang solution for $K < 1.88$ and the increase in drag coefficient for large K because of flow separation at the cylinder. Lu & Ling (2003) studied numerically the three dimensional incompressible sinusoidally oscillating flows past a circular cylinder to analyse vortical instability. They used second order accurate time fractional step method and finite difference/spectral approximations to solve three dimensional incompressible Navier-Stokes equation. Their study showed that three dimensional flow structures along the axial direction appeared because of vortical instability and these structures lie on both sides of the cylinder.

In the present study Navier-Stokes equations were fully resolved in the laminar range, while large-eddy simulation (LES) with the dynamic Smagorinsky model was employed when the flow was turbulent. The basic Smagorinsky model was described by Smagorinsky (1963) and Lilly (1967). Leonard (1974) studied that LES obtained filtered variants of the velocity and the pressure fields, such that the filter width captured the motion scales of the inertia range of the turbulent motion. Further development towards dynamic Smagorinsky model was proposed by Germano *et al.* (1991). The current computations were performed by the LES code which is a modification of CDP code (v2.5.1), this is an unstructured finite volume based CFD code (CITS, 2005), it employs the dynamic

Smagorinsky model, (Ham & Iaccarino, 2004; Ham *et al.*, 2006).

The present work is focused to study numerically in-line forces on a smooth cylinder over a range of frequency parameter β and Keulegan Carpenter number K number. Calculations of the Honji-rolls demonstrated the local flow patterns. These calculations exhibited that the pattern had no consequence for the force on the cylinder. This work also includes the study of regions formed by variation in characteristic parameters. Effort was made to provide data in order to validate Wang analysis as well and to perform LES calculations of flow separation and vortical flow to resolve the flow physics at small scale. These calculations showed that the velocity and vorticity fields contained a large range of motion scales. Evaluation of the frequency contents of the velocity field showed that the energy of the temporal turbulent fluctuations was resolved in the computations.

1.2 Internal Waves

A major type of motion within the fluid rather than on the surface is the internal wave motion. The internal waves are those disturbances that occur at the interface between layers of different densities. This is a widespread phenomenon in oceans, lakes and atmosphere, (Farmer & Smith, 1980; Osborne & Burch, 1980). In atmosphere they create wave clouds whereas in oceans they are the cause of an interesting occurrence of dead water phenomenon. Studies have shown that these waves can be generated by the tidal movement across continental shelves, they can also be caused by turbidity currents, by the pools of light or heavy water masses trapped by wind along complex coastal topographies, (Haury *et al.*, 1979; Maxworthy, 1980; Hibiya, 1988). It is speculated that these waves may thus play an important role in maintaining the large-scale deep circulation, by providing downward mixing of heat. It has been observed that the internal solitary waves (ISWs) can also induce significant currents close to the sea-bed and are thought to enhance rates of suspension of sedimentary material from the sea floor across shore transport of sediments, as studied by Bogucki & Redekopp (2005).

Internal waves manifest themselves on the sea surface in alternating bands of rough and smooth water, which appear as light and dark stripes on satellite images. These stripes can be tens to hundreds of kilometers in length and persist on the surface for several

days as the internal waves move through the ocean. In one of the early studies Apel *et al.* (1975) made an effort to capture images of internal solitary waves between New York and Bermuda, however their study at that time was limited by satellite dynamics and sensor characteristics. Over the past few decades these waves can be visualized by a variety of remote sensing instruments, e.g., ship radar, ground-based radar, photographic camera and imaging radar of airborne etc. and are well documented by Essen *et al.* (1983), Goldstein *et al.* (1989), Gasparovic & Etkin (1994). Satellite SAR (synthetic aperture radar) images record a snapshot view of a vast two-dimensional internal wave field. On the continental shelf and in the coastal ocean an immense range of internal wave behaviour has been intimately projected by SAR profiles for example by Da-Silva *et al.* (1998) and Hsu *et al.* (2000). Figure 5 shows SAR image of Columbia River plume August 2002 taken from Nash & Moum (2005). They studied generation of internal waves from a river plume that flows as a gravity current into the coastal ocean.

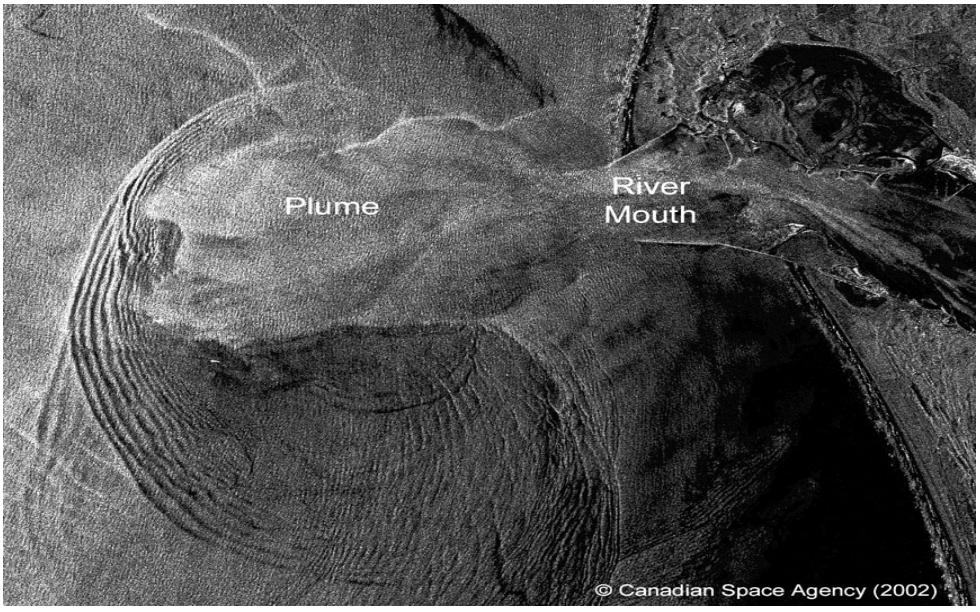

Figure 5: Synthetic aperture radar (SAR) image of the Columbia River plume on 9 August 2002. Image indicates regions of enhanced surface roughness associated with plume-front and internal wave velocity convergences.(Nash & Moum, 2005)

A great deal of work has been theoretically, numerically and experimentally done to describe properties and various characteristics of internal waves. Numerical work by Vlasenko & Hutter (2002) described the transformation of large amplitude internal solitary waves over a slope-shelf topography. In addition to this, the breaking criteria over the slope was also discussed. Helfrich & Melville (2006) provided a detailed description of the properties of steady internal solitary waves and also the transient process of wave generation and evolution. Dotsenko & Shelkovnikov (2009) investigated periodic waves on a slope. They observed the change in wavelength and wave height as it approached the slope. Laboratory and numerical investigations were performed by Fructus *et al.* (2009) in 3-layer stratified systems consisting of two homogeneous layers separated by a linearly stratified pycnocline. They studied the breaking that occurred through shear instability for their experiments. This condition was verified subsequently by Barad & Fringer (2010) and Lamb & Farmer (2010). In one of the recent experimental studies, Carr & Davies (2010) investigated the velocity field close to the bottom boundary and discussed the flow reversal in the rear part of the wave.

Field studies have also been done to record internal waves. Duda *et al.* (2004) and Ramp *et al.* (2004) observed and investigated internal waves in South China Sea along the Continental Slope where ISWs occur very frequently. Duda *et al.* (2004) reported internal solitary waves of depression of amplitude 150m in a water depth of 340m and discussed the propagation of the wave along the slope. Moum *et al.* (2003) studied the large amplitude nonlinear internal waves of depression on the continental shelf of Columbia River. They studied the instabilities associated with the waves in acoustic images suggesting the longitudinal scale of these billow like instabilities. Chen (2012) discussed in detail in-situ observation of internal waves in oceans, estuaries and lakes, by going through the studies done over the past few years from a wide variety of places including Europe, the United States, South Africa, Taiwan, the South China Sea and the Yellow Sea.

The study and identification of the properties and parameters of such waves is very important. Propagation of internal solitary waves, the variation in their properties and breaking phenomenon associated with these waves are cruicial for marine engineering activities in deep water. The internal waves can possibly affect the offshore units connected

by risers or cables to the equipment and wells at the bottom of the sea. This stresses the need to further explore and study the propagation of internal waves and their breaking phenomenon.

1.2.1 Internal waves propagation and breaking

Internal solitary waves propagate on density interface in stratified fluids. They can be waves of depression or waves of elevation depending upon whether the pycnolcine is respectively above or below the mid-depth of the water column. However, they are known to break as a consequence of either convective or shear-driven instability, or by combination of both. In Part 2, from the current set of experiments breaking of internal solitary waves is described, two tanks with dimensions ($12.6\text{m} \times 0.5\text{m} \times 1.0\text{m}$) and ($6.4\text{m} \times 0.4\text{m} \times 0.6\text{m}$) respectively were utilized. By using DigiFlow software Dalziel (2006), particle image velocimetry (PIV) was applied to the digital camera records to extract synoptic velocity and vorticity fields within the illuminated sections. And by overlapping the fields of view of the 3 cameras, it was possible to record and follow simultaneously the behaviour of the wave over at least one full wavelength.

The breaking of ISWs due to shear instability was characterised by the formation of a sequence of rolled vortices (billows). Each of the billows grew with time until arrested by the stratification within the pycnocline, before breaking down to form a turbulent patch. The recordings based upon current experimental setup illustrate the occurrence, growth and decay of a typical billow in a sequence of typically 5-6 identified billows as shown in the figure 6. It was observed that initial perturbation grew with time and developed a characteristic overturning until a recognisable cat's eye-type, closed billow was formed. James Franklin and Stuart King made an effort to simulate the breaking numerically. The numerical model illustrates that billows formed near the trough of the wave, subsequently grew and disturbed the tail.

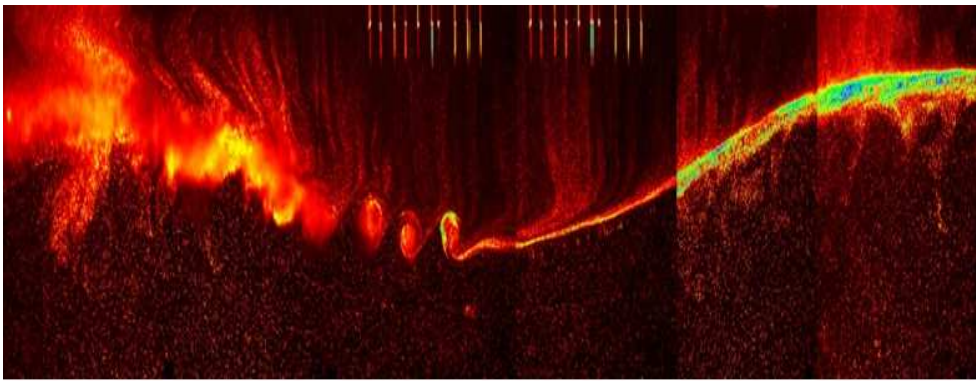

Figure 6: Composite image of breaking internal waves approaching probe assembly (top right)

Observations showed that the behaviour resembles the classic Kelvin-Helmholtz (K-H) instability of the interface between two fluids in parallel motion. However, the temporal and spatial development of the billows in the case of breaking ISWs were affected significantly by the horizontal non-uniformity in velocity within each of the constituent layers. The purpose of this study was to describe measurements of the development of the density field within a breaking ISW billow.

1.2.2 Propagation of Internal Waves over a slope

The focus of Part 3 was internal waves propagating horizontally in a linearly stratified fluid over a slope. This study was based on the experimental work. The aim was to describe the aspects of these waves on the sloping bottom. To investigate the phenomenon an experiment was set up to observe the solitary wave propagation horizontally in a stratified fluid. In the present exprimental study the fluid had a linearly stratified shallow layer above a deep layer of constant density. The density profile was motivated by prevailing conditions in the nature where ISWs are observed.

The experiments were performed in a wave tank at the Hydrodynamics Laboratory of the University of Oslo. The tank is 7m long and 0.25m wide. On one end of the tank a sloping bottom with a slope 0.24m/5.5m (height/length) was installed. Recordings were made at two fields of view (FoV). First illuminated FoV was at a distance of 2.53m from the wall to capture the incoming wave. Position of second illuminated FoV was

5.59m from the wall, which was almost the end of the slope. Both of the illuminated sections had a thickness of approximately 5mm. These illuminated fields of view were seeded with the light reflecting tracer particles of 'Pliolite' having diameter in the range of $355 - 800\mu$m. The particles were treated with a wetting agent for some time in order to get an effective neutral bouyancy for the range of density profile. Motions in these light sheets were viewed and recorded by fixed digital cameras with spatial resolution of 1024×1024 pixels. The field of view for the camera was 20×20cm. It records 100 frames per second and the camera was synchronised with the laser pulse. In all the runs, the recording arrangements were stationary with respect to the tank.

The recorded video of the flow field was processed using the software package DigiFlow to extract velocity field data. Using DigiFlow, Particle Image Velocimetry (PIV) and Particle Tracking velocimetry (PTV) were applied to the digital camera recordings within the illuminated FoVs. PIV and PTV are both powerful experimental methods to extract the velocity field and related dynamics of the waves observed in the tank. PTV was employed for the recordings at second illuminated FoV, i.e. at the slope end. Flow-following particles were introduced into the fuild and their motion was used to estimate the kinematics of the local fluid. For the implementation of PIV and PTV midplanes of the two marked FoVs of the tank were illuminated by ND:YAG laser. ND:YAG laser is a standard light source for recent PIV systems. Its high pulse energy, short pulse duration and adjustable time interval make it ideal for particle imaging. CFR200 (compact folded resonator) systems were used in these runs. The CFR200 PIV systems are designed to supply two laser pulses in rapid succession.

The wave was generated by trapping a volume behind the gate which was lowered at one end of the tank. In the experiments fresh water of density 0.999g/cm^3 was added very gently behind the gate. The corresponding mass of the lower fluid then slowly flowed to the other side of the gate to maintain hydrostatic balance. The trapped volume behind the gate was varied in order to get different input waves. As the gate was removed, a solitary wave of depression propagating along the tank was observed. With the adjustment of the position of the gate along with the depth of the trapped volume a single solitary wave could be generated. Internal waves were recorded for the input volumes of 25, 15, 10 litres respectively.

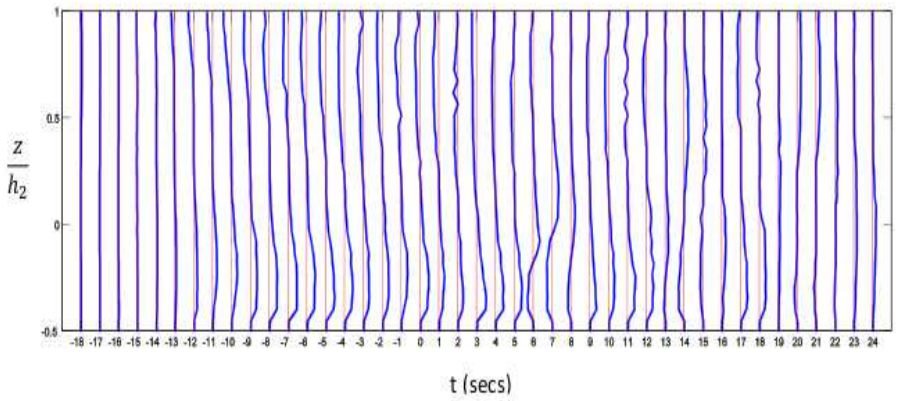

Figure 7: Complete time history of the wave propagating along the slope at FoV-II

The behaviour of the wave as it propagated along the slope was carefully investigated. It was observed that as the wave approached shallow part where the thickness of the lower layer, i.e. h_1 is about 1 to 1.4cm in the middle of the frame, the amplitude of the wave decreased and wave became parallel along the bottom and the length of the wave increased. Ramp *et al.* (2004) in their field study in the South China Sea also reported that as the waves travelled up the continental slope from 350 to 200m depth, the waves had reduced amplitude and the length of the waves increased. The same has been observed in the current study. This variation in internal waves property as they propagate along the slope can also be anticipated by applying ray theory which suggests the change in wavelength as the waves approach shallow region. This gradual change in wave properties while propagating along the slope can be due to dispersion because of the inhomogeneity in the medium. Therefore these variations can be anticipated by ray theory for the current set of experiments. The basic assumption to be satisfied for applying ray theory is that the ratio between the wavelength λ and the inhomogeneous length scale L must be a very small number i.e $\frac{\lambda}{L} \ll 1$. The length scale taken for the present case is the total length of the sloping bottom i.e. 550cm and wavelengths at the first recording section for the present experiments are in the range 20cm to 80cm depending on the initial conditions, hence the condition to apply ray theory is satisfied. The medium for the current study is inhomogenous and stationary. This inhomogenity

embeds itself in the dispersion relation such that the ω is a function of not only the wave number k but also the coordinate x i.e $\omega = \omega(k, x)$. The Ray equations also support the experimental observations in the present study about the modulation of wave relative to the wavelength as the wave propagated along the sloping bottom. This increase in wavelength hence occurred because of inhomogeneity in the medium in the experiments.

In this section effort was also made to describe and document the appearance of boluses as the wave approached the slope end. These boluses were formed at the rear part of the wave where the flow reversal occurred. Figure 7 shows a complete time history at section 2 with input volume of 10 litres. The figure shows the flow reversal occurred at the rear part of the wave at $t = 6$s whereas, first half of the wave showed calm behaviour. Grue & Sveen (2010) also described the formation of boluses when the lower layer thickness became small enough such that it developed into boluses, moving beyond the undisturbed pycnoline-slope intersection. Carr & Davies (2010) reported that the flow reversal occurred at the decelerating part of the wave and no vortices were observed in their experiments performed over a flat bottom. It can be stated that the appearance of these boluses can carry sediments while propagating up the slope , and are also the reason for sediments resuspension. This appearance of boluses and reversal of flow can also cause mixing. Boegman & Ivey (2009) in their experimental study also described the wave induced near bottom vortices to suspend bed material. Southard & Cacchione (1972) reported mixing caused by breaking of internal waves on the slope. Cacchione & Wunsch (1974) in their experimental study of internal waves propagating over a sloping bottom discussed that the shoaling internal waves were capable of suspending and transporting sediments. The present study also agrees with the experimental observations of Helfrich (1992) about wave breaking and production of mutiple boluses and significant vertical mixing at the breaking location.

The work presented in this thesis is believed to be a way forward for the further numerical and empirical study of fluid motion in flow regions from the free surface to the sloping bottom.

.

2

References

An, H., Cheng, L. & Zhao, M. 2011 Direct numerical simulation of oscillatory flow around a circular cylinder at low Keulegan Carpenter number. *J. Fluid Mech.* **666**, 77–103.

Apel, J.R., Byrne, H.M., Proni, J.R. & Charnell, R.L. 1975 Observations of Oceanic Internal and Surface Waves From the Earth Resources Technology Satellite. *J. Geophys. Res.* **80** (6), 865–881.

Apel, J.R., Holbrook, J.R., Liu, A.K. & Tsai, J.J. 1985 The Sulu Sea internal soliton experiment. *J. Phys. Oceanogr.* **15**, 1625–1651.

Barad, M.F. & Fringer, O.B. 2010 Simulations of shear instabilities in interfacial gravity waves. *J. Fluid Mech.* **644**, 61–95.

Boegman, L. & Ivey, G. N. 2009 Flow separation and resuspension beneath shoaling nonlinear internal waves. *J. Geophys. Res.* **114** (C02018).

Bogucki, D.J. & Redekopp, L.G. 2005 Internal solitary waves in the Coastal Mixing and Optics 1996 experiment: Multimodal structure and resuspension. *J. Geophys. Res.* **110**, 1–19.

Cacchione, D. & Wunsch, C. 1974 Experimental study of internal waves over a slope. *J. Fluid Mech.* **66**, 223–239.

Cai, S.Q., Long, X.M. & Gan, Z.J. 2003 A method to estimate the forces exerted by internal solitons on cylindrical piles. *J. Ocean Engineering* **30**, 673 – 689.

Cai, S., Wang, S. & Long, X. 2005 A simple estimation of the force exerted by internal solitons on cylindrical piles. *J. Ocean Engineering* **33**, 974 – 980.

Carr, M. & Davies, P.A. 2010 Boundary layer flow beneath an internal solitary wave of elevation. *Phys. Fluids* **22** (026601).

Chaplin, J.R. 2000 Hydrodynamic damping of a cylinder at "$\beta \approx 10^6$". *J.Fluids and Struct.* **14**, 1101 – 1117.

Chen, C.Y. 2012 A critical review of internal wave dynamics. Part 1-Remote sensing and in-situ observations. *J. Vibration and Control* **18** (3), 417–436.

CITS 2005 Annual technical report. *Tech. Rep.*. Center for Integerated Turbulence Simulations, Stanford.

Da-Silva, J.C.B., Ermakov, S.A., Robinson, I.S., Jeans, D.R.G. & Kijashko, S. V. 1998 Role of surface films in ERS SAR signatures of internal waves on the shelf 1. Short-period internal waves. *J. Geophys. Res.* **103**, 8009–8031.

Dotsenko, S. & Shelkovnikov, N. 2009 Laboratory modeling of the propagation of periodic internal waves over bottom slopes. *J. Phys. Oceanogr.* **19**, 301–309.

Duda, T.F., Lynch, J.F., Irish, J.D., Beardsley., R.C., Ramp, S.R., Chiu, C.S., Tang, T.Y. & Yang, Y.J. 2004 Internal tide and nonlinear internal wave behavior at the continental slope in the northern south China Sea. *IEEE, J. Oceanic Engineering* **29**, 1105–1130.

Ekman, V.W. 1904 On dead water. In Norwegian north polar expedition, 1893-1896. Scientific results. *ed F. Nansen* **5**.

Essen, H.H., Schirmer, F. & Sirkes, S. 1983 Acoustic remote sensing of internal waves in shallow water. *Int. J.Remote Sensing* **4**, 33–47.

Farmer, D.M. & Smith, J.D. 1980 Tidal interaction of stratified flow with a sill in Knight Inlet. *Deep-Sea Res.* **27**, 239–254.

Fructus, D., Carr, M., Grue, J., Jensen, A. & Davies, P.A. 2009 Shear-induced breaking of large internal solitary waves. *J. Fluid Mech.* **620**, 1–29.

Gasparovic, R.F. & Etkin, V.S. 1994 An overview of the Joint US/Russia Internal Wave Remote Sensing Experiment. In *IGARSS '94. Digest.*, , vol. 2, pp. 741 – 743.

Gavrilov, N. & Ermanyuk, E. 1996 Effect of a pycnocline on forces exerted by internal waves on a stationary cylinder. *J. App. Mechanics and Tech. Phys.* **37**, 825–831.

Germano, M., Piomelli, U., Moin, P. & William, H.C. 1991 A dynamic subgrid-scale eddy viscosity model. *Phys. Fluids* **3**, 1760–1765.

Goldstein, R.M., Zebker, H.A. & Barnett, T.P. 1989 Remote Sensing of Ocean Currents. *Science* **246**, 1282–1285.

Grue, J., Jensen, A., Rusås, P. & Sveen, J.K. 1999 Properties of large-amplitude internal waves. *J. Fluid Mech.* **380**, 257–278.

Grue, J., Rashid, F. & Vartdal, M. 2011 Oscillating cylinder in viscous fluid: calculation of flow patterns and forces. *J. Engineering Mathematics* **70** (1), 281–295.

Grue, J. & Sveen, J. K. 2010 A scaling law of internal run-up duration. *Ocean Dynamics* **60**, 993–1006.

Hall, P. 1984 On the stability of the unsteady boundary layer on a cylinder oscillating transversely in a viscous fluid. *J. Fluid Mech.* **146**, 347–367.

Ham, F. & Iaccarino, G. 2004 Energy conservation in collocated discretization schemes on unstructured meshes. *Centre for Turbulence Research, Stanford* .

Ham, F., Mattasson, K. & Iaccarino, G. 2006 Accurate and stable finite volume operators for unstructured flow solvers. *Centre for Turbulence Research, Stanford* .

Haury, L.R., Briscoe, M.G. & Orr, M.H. 1979 Tidally generated internal wave packets in Massachusetts Bay. *Nature* **278**, 312–317.

Helfrich, K.R. 1992 Internal solitary wave breaking and run-up on a uniform slope. *J. Fluid Mech.* **243**, 133–154.

Helfrich, K.R. & Melville, W.K. 2006 Long nonlinear internal waves. *Ann. Rev. Fluid Mech.* **38**, 395–425.

Hibiya, T. 1988 The Generation of Internal Waves by Tidal Flow Over Stellwagen Bank. *J. Geophys. Res.* **93**, 533–542.

Honji, H. 1981 Streaked Flow around an oscillating circular-cylinder. *J. Fluid. Mech.* **107**, 509–520.

Hsu, M.K., Liu, A.K. & Liu, C. 2000 A study of internal waves in the China Seas and Yellow Sea using SAR. *Continental Shelf Research* **20**, 389–410.

Johanning, L., Bearman, P.W. & Graham, J.M.R. 2001 Hydrodynamic damping of a large scale surface piercing circular cylinder in planar oscillatory motion. *J. Fluids and Struct.* **15**, 891–908.

Keulegan, G.H. & Carpenter, L.H. 1958 Forces on Cylinders and Plates in an Oscillating Fluid. *J.Res.Bur.Stand* **60**, 423–440.

Lamb, K.G. 1994 Numerical experiments of internal wave generation by strong tidal flow across a finite amplitude bank edge. *J.Geophysical Res.* **99**, 843–864.

Lamb, K.G. & Farmer, D. 2010 Instabilities in an Internal Solitary-like Wave on the Oregon Shelf. *J. Phys. Oceanogr.* **41**, 67–87.

Leonard, A. 1974 Energy cascade in large eddy simulation of turbulent fluid flow. *Adv. Geophys.* **18A**, 237–248.

Lilly, D.K. 1967 The representation of small-scale turbulence in numerical simulation experiments. *In H.H Goldstine (Ed), Proc.IBM, Scientific Computing Symp.On Environmental Sciences* pp. 195–210.

Lu, X., Dalton, C. & Zhang, J. 1997 Application of Large Eddy Simulation to an oscillating flow past a circular cylinder. *J.Fluids Engg.* **119**, 519–525.

Lu, X.Y. & Ling, G.C. 2003 Three-dimensional instability of an oscillating viscous flow past a circular cylinder. *App.Math. and Mech. Engg. Ed.* **24** (7), 791–800.

Maxworthy, T. 1980 On the formation of nonlinear internal waves from the gravitational collapse of mixed regions in two and three dimensions. *J. Fluid Mech.* **96**, 47–64.

Morison, J.R., O'Brien, M.P., Johnson, J.W. & Schaff, S.A.. 1950 Forces exerted by surface waves on piles. *Petrol. Trans., Am.Inst.Mining Eng* **189**.

Moum, J.N., Farmer, D.M., Smyth, W.D., Armi, L. & Vagle, S. 2003 Structure and Generation of Turbulence at Interfaces Strained by Internal Solitary Waves Propagating Shoreward over the Continental Shelf. *J. Phys. Oceanogr.* **33**, 2093–2112.

Nansen, F. 1905 The Norwegian north polar expedition 1893-1896 scientific results **4** (13), 232.

Nash, J.D. & Moum, J.N. 2005 River plumes as a source of large-amplitude internal waves in the coastal ocean. *Nature* **437**, 400–403.

Osborne, A.R. & Burch, T.L. 1980 Internal Solitons in the Andaman Sea. *Science* **208**, 451–460.

Otter, A. 1990 Damping forces on a cylinder oscillating in a viscous fluid. *Appl. Ocean Res.* **12**, 153 – 155.

Ramp, S.R., Tang, T.Y., Duda, T.F., Lynch, J.F., Liu, A.K., Chiu, C.S., Bahr, F.L., Kim, H.R. & Yang, Y.J. 2004 Internal solitons in the northeastern south China Sea. Part I: sources and deep water propagation. *IEEE, J. Oceanic Engineering* **29**, 1157–1181.

Sadeghi, K. 2007 An Overview of Design, Analysis, Construction and Installation of Offshore Petroleum Platforms Suitable for Cyprus Oil/Gas Fields. *GAU J. Soc and Appl. Sci.* **2(4)**.

Sarpkaya, T. 1986 Force on a circular-cylinder In Viscous Oscillatory Flow At Low Keulegan-Carpenter Numbers. *J. Fluid Mech.* **165**, 61–71.

Smagorinsky, J. 1963 General circulation experiments with the primitive equations. *Monthly Weather Review* **91** (3), 99.

Song, Z.J., Teng, B., Gou, Y., Lu, L., Shi, Z.M., Xiao, Y. & Qu, Y. 2011 Comparisons of internal solitary wave and surface wave actions on marine structures and their responses. *Applied Ocean Research* **33**, 120–129.

Southard, B. & Cacchione, D. A. 1972 Experiments on bottom sediment movement by breaking internal waves. In *Shelf Sediment Transport: Process and Pattern* (ed. D. J. P. Swift, D. B. Duane & O. H. Pilkey), pp. 83 – 98. Geological Society of America.

Stokes, G. 1851 On the effect of the internal friction of fluids on the motion of pendulums. *Trans. Camb. Phil. Soc.* **9**, 8–106.

Suthon, P. & Dalton, C. 2012 Observations on the Honji instability. *J. Fluids and Structures* pp. 27–36.

Vlasenko, V. & Hutter, K. 2002 Numerical experiments on the breaking of solitary internal waves over a slope shelf topography. *J. Phys. Oceanogr.* **32**, 1779–1793.

Wallace, B.C. & Wilkinson, D.L. 1988 Run-up of internal waves on a gentle slope in a two-layered system. *J. Fluid Mech.* **191**, 414–442.

Wang & Chang, Y. 1968 On high-frequency oscillatory viscous flows. *J. Fluid Mech.* **32**, 55–68.

Wu, J.Z., Lu, X.Y. & Zhuang, L.X. 2007 Integral forces acting on a body due to local flow structures. *J. Fluid Mech.* **576**, 265–286.

PART I

J Eng Math (2011) 70:281–295
DOI 10.1007/s10665-010-9395-7

Oscillating cylinder in viscous fluid: calculation of flow patterns and forces

Farah Rashid · Magnus Vartdal · John Grue

Received: 9 April 2010 / Accepted: 12 July 2010 / Published online: 5 August 2010

Abstract Laminar and large-eddy-simulation (LES) calculations with the dynamic Smagorinsky model evaluate the flow and force on an oscillating cylinder of diameter $D = 2R$ in otherwise calm fluid, for $\beta = D^2/\nu T$ in the range 197–61400 and Keulegan–Carpenter number $K = U_m T/D$ in the range 0.5–8 (ν kinematic viscosity, T oscillation period, U_m maximal velocity). Calculations resolving the streakline patterns of the Honji instability exemplify the local flow structures in the cylinder boundary layer ($\beta \sim 197$–300, $K \sim 2$) but show that the drag and inertia force are not affected by the instability. The present force calculations conform with the classical Stokes–Wang solution for all cases below flow separation corresponding to $K < 2$ (with $\beta < 61400$). The LES calculations of flow separation and vortical flow resolve the flow physics containing a large range of motion scales; it is shown that the energy in the temporal turbulent fluctuations (in fixed points) are resolved. Accurate calculation of the flow separation occurring for $K > 2$ has strong implication for the force on the cylinder. Present calculations of the force coefficients for K up to 4 and $\beta = 11240$ are in agreement with experiments by Otter (Appl Ocean Res 12:153–155, 1990). Drag coeffients when flow separation occurs are smaller than found in U-tube experiments. Inertia coefficients show strong decline for large K (up to 8) and moderate $\beta = 1035$ but is close to unity for $K = 4$ and $\beta = 11240$. The finest grid has 2.2×10^6 cells, finest radial $\Delta r/R = 0.0002$, number of points along the cylinder circumference of 180, $\Delta z/R = 0.044$ and a time step of $0.0005T$.

Keywords Flow physics · Flow separation · Honji instability · LES calculation · Smagorinsky

1 Introduction

Many papers have considered the forces on a long cylinder exposed to oscillatory flow, including, particularly, a group of classical papers by Stokes [1], Wang [2], Honji [3] and Hall [4], experimental papers by e.g. Sarpkaya [5], Otter [6], Chaplin [7], Sarpkaya [8], Johanning et al. [9] and Chaplin and Mouazé [10], and (quite) recent computational papers by Lu et al. [11], Lu and Ling [12] and Wu et al. [13]. A combined experimental and computational study was given by Dütsch et al. [14]. In the very recent paper by An et al. [15] detailed computations and flow visualizations of Honji vortices below flow separation are provided. The present paper falls into the category of computations. We compute the flow and forces on a long cylinder that oscillates in a fluid otherwise at rest. The

F. Rashid · M. Vartdal · J. Grue (✉)
Mechanics Division, Department of Mathematics, University of Oslo, Oslo, Norway
e-mail: johng@math.uio.no

calculations are performed for ranges of the β-number, Keulegan–Carpenter number (K) and Reynolds number (Re). β is up to 61400, K up to 8 and Re up to 45000.

The Navier–Stokes equations are fully resolved in the laminar flow range, while large-eddy simulation (LES) is employed when the flow is turbulent. LES obtains filtered variants of the velocity and pressure fields, assuming that the filter width captures the motion scales of the inertia range of the turbulent motion [16]. Pioneering works on LES include the original Smagorinsky model of the sub-grid scale (SGS) motion [17,18]. Notable are the development and success of the dynamic Smagorinsky model, as proposed by Germano et al. [19] and further extended by Lilly [20] and Meneveau et al. [21]. Thanks to the steadily increasing computer power, the computational challenge with LES is merely how it best can be performed, rather than how it can be afforded. For recent references on SGS closure and LES, see the book by Pope [22] and the review by Pope [23].

In this paper we describe LES and laminar-flow computations solving the plain or filtered Navier–Stokes equations. The computations are carried out using an extension of the CDP code (v2.5.1), which is an unstructured finite-volume based CFD code developed at Stanford University's Centre for Integrated Turbulence Simulations (CITS) over a period of 10 years. It has been applied to a variety of complex fluid-mechanical problems, including: staggered jet in cross-flow, flow in jet-engine fuel-nozzle rig and full wheel combustor simulation [24,25]. The code emphasizes good kinetic energy-conservation properties, which is a necessity for accurate turbulence simulations [26]. Implementation details can be found in [27].

The present effort represents a first step towards a long-term goal, which is to extend the LES code to free-surface motion and the interaction with marine bodies. An important example includes nonlinear wave diffraction from slender vertical cylinders (offshore wind turbines) where a typical diameter may be 5 m, wave amplitude up to 18.5 m (corresponding to the crest height of the Draupner wave), implying a Keulegan–Carpenter number up to about 20. The estimate indicates a need to resolve both flow separation and wave breaking at the geometry.

1.1 Circular cylinder in sinusoidal flow

Sinusoidally oscillating flow past a fixed circular cylinder has acquired a great deal of attention from fluid dynamicists and engineers because of its theoretical significance and practical importance. The forces acting on a general body are assumed to be the sum of the inertia force, viscous force and drag. The total force can be expressed in terms of Morison's equation which for a long circular cylinder of diameter D takes the form

$$F = \tfrac{1}{4}\pi\rho D^2 C_m \dot{U} + \tfrac{1}{2}\rho D C_d |U| U. \tag{1}$$

Here, ρ denotes the density of the fluid and $U = U_m \sin(2\pi t/T)$ the velocity of the flow, with T the period. By (1) the force is represented by the inertia coefficient C_m and drag coefficient C_d. The oscillatory flow can be characterised by two parameters, viz. the Keulegan–Carpenter number defined by $K = U_m T/D$, indicating the ratio between the convective and local acceleration, and the Reynolds number defined by $\mathrm{Re} = U_m D/\nu$ where ν denotes the kinematic viscosity. Alternatively, Re is replaced by a frequency parameter β defined by $\beta = D^2/\nu T = \mathrm{Re}/K$. Reference to the Stokes number St in place of the β-number is sometimes used ($\mathrm{St} = \beta$); see below.

Stokes [1] was the first to show that the force on a fixed cylinder exposed to a sinusoidal flow of a viscous fluid is dependent on both K and Re. Wang [2], using the method of inner and outer expansions, extended Stokes' analysis. The Stokes–Wang solution valid for $K \ll 1$, and $\beta \gg 1$, can be reduced to the following form

$$C_d = \frac{3\pi^3}{2K}\left[(\pi\beta)^{-\frac{1}{2}} + (\pi\beta)^{-1} - \tfrac{1}{4}(\pi\beta)^{-\frac{3}{2}}\right], \tag{2}$$

$$C_m = 2 + 4(\pi\beta)^{-\frac{1}{2}} + (\pi\beta)^{-\frac{3}{2}}. \tag{3}$$

If the cylinder is oscillating in a fluid otherwise at rest, like in the present calculations, the inertia coefficient is expressed by $\hat{C}_m = 1 + 4(\pi\beta)^{-\frac{1}{2}} + (\pi\beta)^{-\frac{3}{2}}$.

In an experimental glass-tank facility with fluid otherwise at rest, Honji [3] oscillated back and forth a vertical circular cylinder of height $H = 30$ cm and diameter D, the latter ranging between 2 and 3.8 cm, such that $H/D \gg 1$.

He described a three-dimensional instability of the flow appearing in the form of an oscillatory cell pattern in the boundary layer of the oscillating cylinder. The cylinder motion was given by $\frac{1}{2}d(t) = \frac{1}{2}d_0 \sin(2\pi f t)$, with $\frac{1}{2}d_0$ the amplitude and $f = 1/T$ the frequency. In his original work Honji expressed the appearance of the instability in terms of the non-dimensional amplitude d_0/D and Stokes number $\mathrm{St} = fD^2/\nu$. (The St-number equals the β-number.) Investigating the range $0.4 < d_0/D < 1.2$ and $70 < \mathrm{St} < 700$ he identified the domain where the cell pattern appeared: for relatively large St, exceeding about 400, the cell pattern appeared for amplitudes in the range, about $0.4 < d_0/D < 0.7$. For smaller Stokes number, upper and lower bounds of d_0/D both increased, however, with the same difference $(d_0/D)_{\max} - (d_0/D)_{\min}$, approximately. The behavior of the cells exhibited locally a mushroom-like streakline pattern. Honji found no regular patters for d_0/D above the upper bound where the flow exhibited flow separation and turbulence.

While the present work was in progress, An et al. [15] have, by means of a finite-element method, provided detailed simulations and flow visualizations of the Honji vortices, for $K = 2$ and $\beta \sim 100$–600. They were able to identify steady-streaming structures induced by the Honji rolls.

Performing U-tube measurements with a cylinder at rest, but oscillating the water, for β-numbers in the range between 1035 and 11240, Sarpkaya [5] has maintained that presence of the Honji instability along the cylinder boundary causes a drag force that is higher than predicted by the Stokes–Wang solution (2). This has, however, not been found in experiments with a smooth cylinder oscillating in still water. With $\beta = 61400$, Otter [6] showed that the damping forces are close to the Stokes–Wang solution for $K < 1.88$ and that the drag coefficient then increases for larger K because of flow separation at the cylinder. In Otter's experiment, theoretical instability value of transition to Taylor–Görtler instability [4] occurred at a Keulegan–Carpenter number of 0.37. The present numerical calculations of C_d and C_m agree with Otter's experimental values. Moreover, we find in the regime of the Honji rolls, that their appearance do not change the force coefficient C_d. This is the same both prior to and after their appearance.

Chaplin and Mouazé [11] have presented a collection of available experimental measurements of the drag coefficient for $100 < \beta < 2 \times 10^6$ and K (about) below the theoretical stability bound of Taylor–Görtler vortices given by Hall [4]. Experiments by Otter [6] and one of the data sets by Johanning [28] exhibit drag coefficients corresponding to the Stokes–Wang solution (JR Chaplin (2010), personal communication). This is also true for parts of the data set of Sarpkaya [5]. An unpublished experimental data set for $\beta = 20000$ showed $C_d/W \sim 1.03$–1.18 (W meaning the Stokes–Wang C_d), and computational attempts showed similar forces (JR Chaplin (2010), personal communication). Other experimental, sets included in Chaplin and Mouazé's summary [10] showed drag coefficients twice the Stokes–Wang solution [7,8,28–30]. A problem with the U-tube experiments, where the cylinder is fixed and the water oscillating, is that the input flow may become polluted by boundary-layer effects and turbulence. The scatter in C_d at high values of β and small K remains an experimental and computational challenge.

The paper is organized as follows. Following the introduction, Sect. 2 describes the numerical code, its implementation, discretization aspects and organization of the computations. In Sect. 3 detailed computations of the Honji instability and the particular mushroom-shaped flow patterns in the cylinder boundary layer are presented. Calculations of the forces, obtaining the inertia and drag coefficients are discussed in Sect. 4 as well as comparison to other force calculations and measurements. A short Sect. 5 discusses the highly local and three-dimensional flow pattern occurring during flow separation, exemplifying also the frequency components of the velocity field. Finally, a conclusion is given in Sect. 6. A description of the particular implementation of the dynamic Smagorinsky model is found in the Appendix.

2 Numerical approach

In this investigation the motion is modeled in a frame of reference $O - x, y, z$ fixed to the oscillating cylinder. The z-axis coincides with the cylinder axis, x-axis is along the oscillatory cylinder motion, y-axis in the lateral direction, and the plane $z = 0$ midways on the cylinder vertical. Coordinates (x, y, z) or alternatively (x_1, x_2, x_3) are used.

For the present calculations a modified version of the CDP 2.5.1 code is employed [27]. It is an unstructured finite-volume node-based code designed for large-eddy simulation (LES) for potentially very large grids using parallel computers. For the present calculations, the incompressible Navier–Stokes version of CDP is modified with a source term in order to incorporate the moving frame of reference of the cylinder. Additionally, for LES, we are using the dynamic Smagorinsky model (see Appendix). This results in the following set of equations

$$\frac{\partial \overline{U}_j}{\partial x_j} = 0, \tag{4}$$

$$\frac{\mathrm{D}\overline{U_j}}{\mathrm{D}t} = \nu \frac{\partial^2 \overline{U}_j}{\partial x_i \partial x_i} - \frac{\partial t^r_{ij}}{\partial x_i} - \frac{1}{\rho}\frac{\partial \overline{p}}{\partial x_j} + S\delta_{1j}, \tag{5}$$

where $\overline{U}_j$ denotes the filtered velocity, $\overline{p}$ the filtered pressure and t^r_{ij} the residual-stress tensor. The latter is expressed in terms of the dynamic Smagorinsky model; see the Appendix. Further, S is the source term applying along the x-direction given by

$$S = \omega U_m \cos(2\pi t/T), \tag{6}$$

where U_m is the maximum velocity of the cylinder as defined in the Sect. 1.1 above ($\omega = 2\pi/T$). All the discretizations of the terms above are found in [27] except for the source term which is discretized according to

$$\int_{V_P} S \mathrm{d}V_P = SV_P, \tag{7}$$

where V_P is the dual control volume of the node P.

2.1 Discretization aspects and organization of computations

We have made fourteen runs, a–k, some with different resolutions (runs b1,2 and j1,2,3), see Tables 1 and 2. The cylinder has radius R and height H; this is $6R$, however, an additional run c of the Honji instability is made with $H = 8R$ (Table 1), as well as a convergence run k with $H = 4R$ for high values of β and K (Table 2). The computational domain is represented by a box of dimensions $(60R, 20R, 6R)$ in (x, y, z), with periodic extensions in all directions.

In runs a,b,c of the Honji instability, for $\beta = 197$ and 300 (Table 1), the discretization along the vertical is $\Delta z/R = 0.1$. The total number of cells in these runs is $0.8–1.1 \times 10^6$. In runs d-j $\Delta z/R = 0.086$ and run k $\Delta z/R = 0.044$ (Table 2). In the angular direction 128 points are used in runs a-j2,k and 180 in run j3. In the radial direction the grid cell nearest to the cylinder boundary is $\Delta r/R = 0.001$ (runs a–c), $\Delta r/R = 0.0004$ (d–g,i,j1) and $\Delta r/R = 0.0002$ (j2,j3,k) (Table 2).

The discretization along the plane $z = 0$ is shown in Fig. 1 (runs j2,k). Plot a shows the section of the entire computational domain, with totally 1.5×10^6 sub-volumes; color plot b shows a magnification of the discretization at the cylinder boundary, including computational results of the velocities and velocity shear in the boundary layer, at $(x, y, z) = (0, R, 0)$, and plot c shows a stronger magnification. The computation shown in color Fig. 1b has parameters $K = 4$, $\beta = 11240$. Convergence tests are performed for $K = 4$, $\beta = 11240$ using a coarser grid with 1.2×10^6 cells (run j1) and finer one with 2.2×10^6 cells (run j3). In the runs with $K = 4$ the time step is $0.0005T$, in all other runs it is $0.001T$.

Table 1 Wavelength of Honji mushroom $\frac{\lambda}{D}$

Run	H	(β, K)	Present	Honji	Lu and Ling	An et al.
a	$6R$	(300, 2)	0.5	0.6	0.59	∼0.6–0.7
b1,2	$6R$	(197, 2.07)	0.6	0.63	–	∼0.6–0.7
c	$8R$	(197, 2.07)	0.67	0.63		∼0.6–0.7

Table 2 Force coefficients for different values of β and K

Run	β	K	$\hat{C}_m$	$(\hat{C}_m+1)/W$	C_d	C_d/W
a	300	2.0	1.108	0.989	1.036	1.101
b1,2	197	2.07	1.135	0.989	0.868	1.104
d	1035	2.5	1.017	0.975	0.577	1.742
e	1035	4.86	0.856	0.896	0.919	5.391
f	1035	6.28	0.780	0.844	1.125	8.515
g	1035	8.0	0.566	0.753	1.335	12.89
h	11240	1.0	1.025	1.002	0.228	0.930
i	11240	2.0	1.013	0.996	0.184	1.498
j1,2,3	11240	4.0	0.95	0.97	0.36	5.83
k	61400	0.5	1.016	1.003	0.187	0.890

W means Stokes–Wang solution given in (2–3)

The simulations were carried out at the University of Oslo on a computer with 16 cores operating at 2.13 GHz. The simulation time for each case was in the order of 1 week.

3 Simulations of the Honji rolls

In the laminar range, secondary streaming is generated in the cylinder's boundary layer. For sufficiently large oscillation amplitude (and Keulegan–Carpenter number), roll pattern becomes generated, superposed on this streaming, as experimentally found by Honji [3]; see Sect. 1.1, and also in recomputations by Lu and Ling [12] and An et al. [15]. Below we shall compare the present computations to those found in [11,12,15]. The roll pattern extends vertically along the cylinder boundary and has a maximum in the plane $x = 0$. The roll pattern is periodic with period $\frac{1}{2}T$, with maxima at $2\pi t/T = 0, \pi, 2\pi$ etc. The cycle of the z-velocity w is visualized in color Fig. 2 for $K = 2.07, \beta = 197$ (finest run b in Table 1), showing the rolls for $2\pi t/T = 0, \pi/4, \pi/2$. At the latter time the rolls almost disappear before gaining again, keeping the polarity. This computation is well within the domain where the cell pattern appeared in Honji's experiments, with range $0.4 < d_0/D < 1.2$ (corresponding to $1.26 < K < 3.77$) and $70 < \beta = \mathrm{St} < 700$.

Putting the perturbation velocities in the plane $x = 0$ on the form $(v, w) = (\partial\psi/\partial z, -\partial\psi/\partial y)$ the stream function ψ may be integrated, where $\psi =$ constant gives streak lines of the mushroom-shaped instability as visualized in color Fig. 3. The calculations compare well to the experimental measurements by Honji [3] (Fig. 4). The height of the mushroom is $h = 0.65R$; the outer width is $W_o = 0.62R$ and inner width $W_i = 0.4R$. With a number of five mushrooms appearing along the cylinder length of $6R$, the wavelength of the instability becomes $\lambda/D = 0.6$ in this case. We have carried out four runs simulating the Honji instability as indicated in Table1 by runs a, b1, b2 and c, for (β, K) values of (300, 2) and (197, 2.07). The difference between runs b1 and b2 is that two different resolutions are used. In run c the cylinder of height $8R$ is used; in this case the wavelength of the instability becomes $\lambda/D = 0.67$. Both computations agree with Honji's observation of the wavelength, obtained for two cylinders of diameters 2 and 3.8 cm, both of height 30 cm; see his Fig. 14. The calculations by Lu and Ling [12] show a wavelength of 0.59 when their cylinder becomes tall, while An et al. [15] have found $\lambda/D \sim 0.6$–0.7, see their Fig. 24.

4 Force calculations

The pressure and shear force are integrated over the cylinder surface during the simulation time which is up to $23T$, as illustrated in Fig. 5a for run b1 with $(\beta, K) = (197, 2.07)$. After about $t = 2T$ the force is almost repeatable—before this time small transients are present. After a time $t = 14T$ the small instabilities appear at the surface

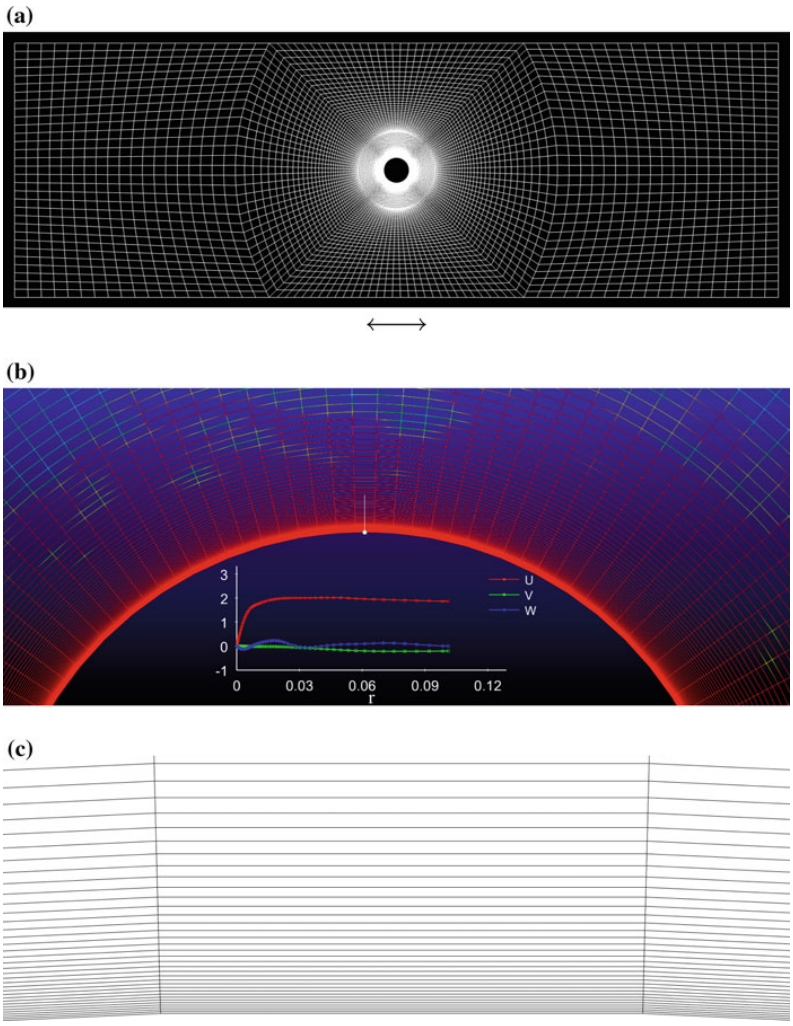

Fig. 1 Example of discretization. Plain cut of mid-section. Total number of cells 1.5×10^6. *Arrows* indicate cylinder motion. **a** Complete lateral extension. **b** Cells at the cylinder in moderate close-up. Also shown are velocities $(u, v, w)/U_\infty$ along the radial direction, at the widest part of the cylinder. **c** Cells at the cylinder in strong close-up. Innermost cell has $\Delta r/R = 0.0002$

of the body; in the present calculations they first appear at the intersection between the cylinder surface and the periodic boundaries at $z = \pm 3R$. The instabilities grow along the cylinder surface towards $z = 0$, from both sides, developing into the rolls and mushroom-shaped instabilities discussed above. An important result of the simulations is that the presence of the Honji instability does not change the drag coefficient. Apart from some initial transients, the value of C_d is the same both before and after the instability appears.

Figure 5b illustrates the force history for runs j1 and j2 for time up to $13T$, both with $(\beta, K) = (11240, 4)$. Run j1 marked with the dashed line has 1.2×10^6 cells, while j2 marked with the solid line has 1.5×10^6 cells. Apart from a small difference during the initial phase, the force histories are identical. Due to the separation taking place at the cylinder, the flow is not entirely symmetric, causing a lateral force acting on the cylinder. This is shown in

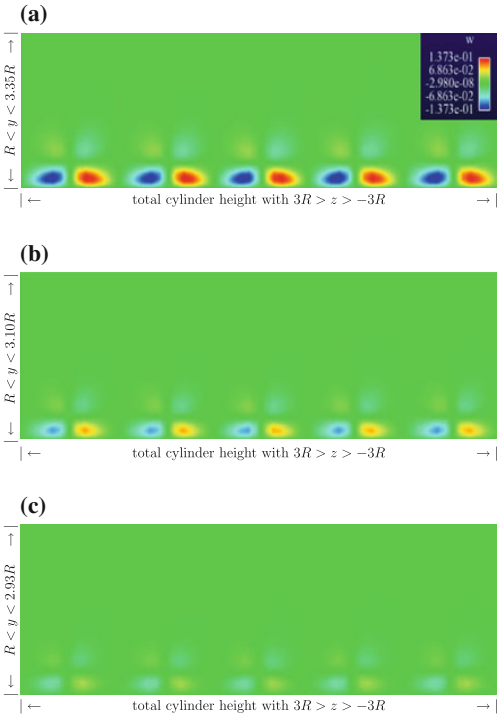

Fig. 2 The cycle of the z-velocity w in $x = 0$ plane, at the total z-direction of the cylinder. $K = 2.07$, $\beta = 197$. $t = 0$ (**a**), $2\pi t/T = \pi/4$ (**b**) and $2\pi t/T = \pi/2$ (**c**)

Fig. 5c for runs j1 and j2. It is noted that the transverse force is much smaller than the in-line force. More precisely, F_y/W has rms of 0.021 and 0.022 relative to the max F_x/W in runs j1 and j2, respectively, for $(\beta, K) = (11240, 4)$.

Altogether, we have performed fourteen different computational runs evaluating the flow and force characteristics and thereby extracting the force coefficients according to the Morison equation (1); see Table 2. We have already noted one surprise, namely for the runs in the Honji instability range, where the drag force remained unchanged and close to the Stokes–Wang solution. This has also been true for the other runs, for the larger values of β, but with K small enough to avoid flow separation ($K < 2$). In this range present computed drag coefficients are close to the Stokes–Wang solution, as visualized in Fig. 5d.

For the runs when flow separation is dominant, three runs e,f,g, all with $\beta = 1035$, and $K = 4.86, 6.28, 8$ show drag coefficients $C_d = 0.919, 1.1125, 1.335$ and inertia coefficients $\hat{C}_m = 0.856, 0.780, 0.566$, respectively (Re up to 8280), i.e., a strong increase in C_d and a strong decline in $\hat{C}_m$ (Table 2; Fig. 5e).

In runs j1,2,3, with the much higher $\beta = 11240$ and $K = 4$ (and Re $= 45000$), the present calculation of the drag coefficient becomes $C_d = 0.36$. This C_d-value is in excellent agreement with the measurements of C_d performed by Otter [6] of cylinders oscillating in water otherwise at rest, finding $C_d = 0.31$ for $(\beta, K) = (61400, 3.63)$ and $C_d = 0.44$ for $(\beta, K) = (61400, 4.22)$.

In runs j1,2,3 with $(\beta, K) = (11240, 4)$ there is not a big drop in the inertia coefficient, which becomes $\hat{C}_m = 0.95$.

4.1 Comparison to other force calculations and measurements

Results of the drag coefficient, particularly in two publications, are relevant to compare with and discuss. These are the LES simulations by Lu et al. [11] and the U-tube experiments by Sarpkaya [5]. In Lu et al. they simulated

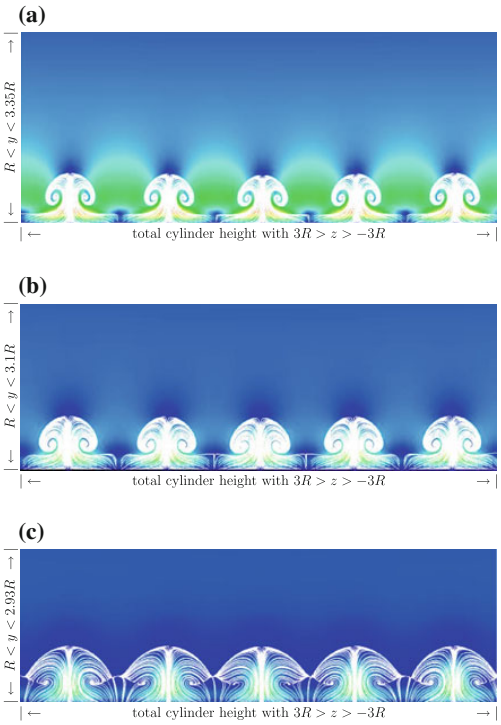

Fig. 3 'Mushroom' vortices corresponding to the Honji instability in $x = 0$ plane, along the total z-direction of the cylinder. $K = 2.07$, $\beta = 197$. $t = 0$ (**a**), $2\pi t/T = \pi/4$ (**b**) and $2\pi t/T = \pi/2$ (**c**)

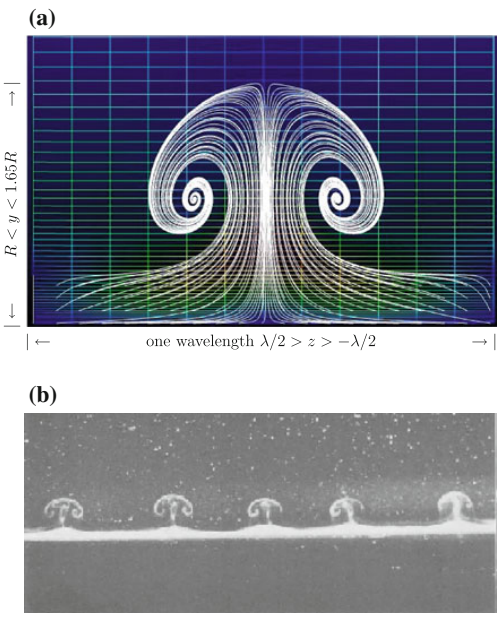

Fig. 4 **a** Expansion of a single roll in Fig. 3a. Number of grid cells 1.5×10^6. **b** Close-up view of streaked flow on cylinder. $K = 2.07$, $\beta = 197$. Adapted from [3, Fig. 10]

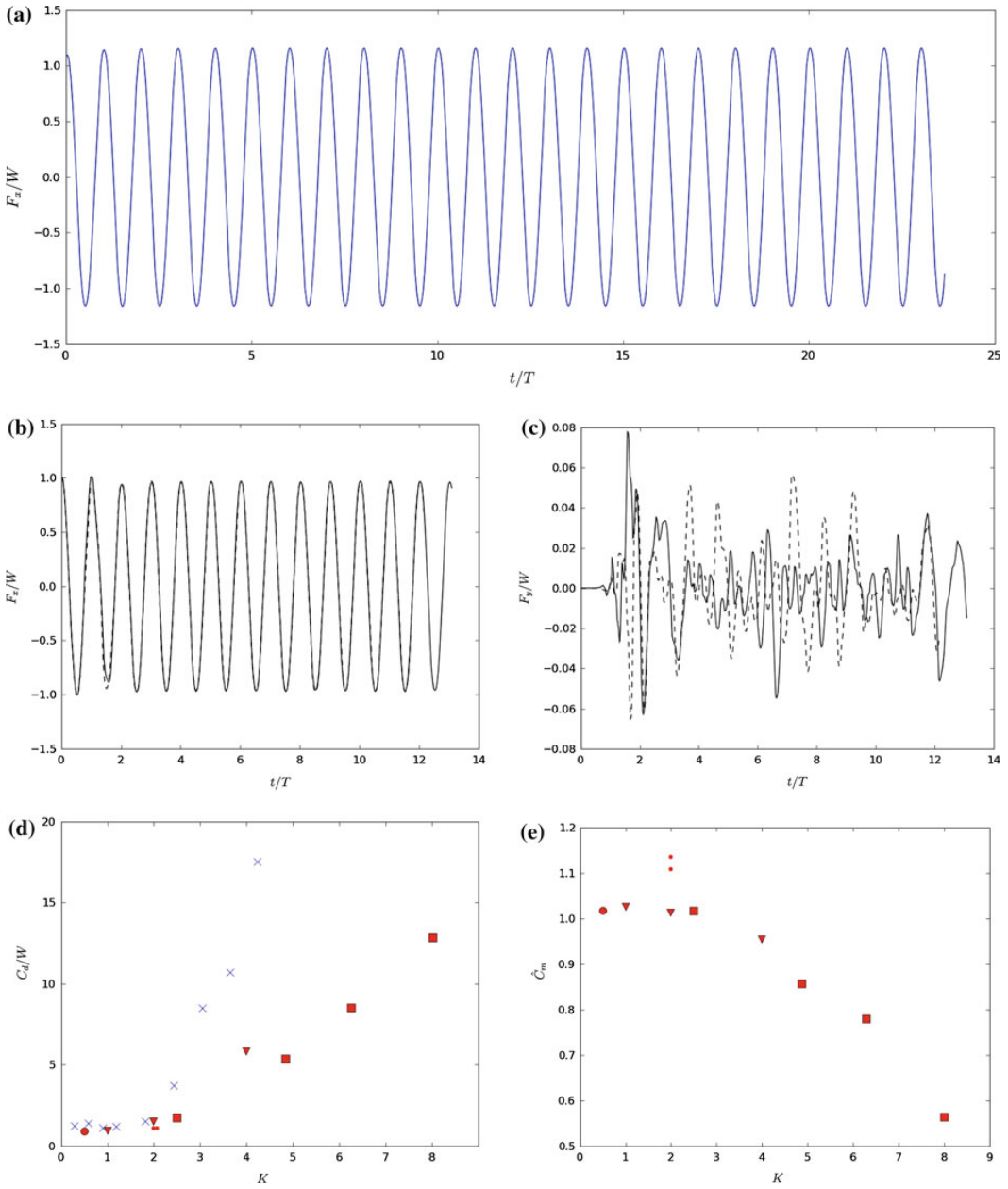

Fig. 5 Force history (along x-direction) normalized by Stokes–Wang solution (inertia coefficient) **a** run b1 with $(\beta, K) = (197, 2.07)$; **b** run j1 (*dashed*); run j2 (*solid*) with $(\beta, K) = (11240, 4)$; **c** lateral force along y-direction in run j1 (*dashed*); run j2 (*solid*); **d** drag coefficient divided by Stokes–Wang solution denoted by W versus K. Present with $\beta = 61400$ (*large circle*); $\beta = 11240$ (*triangle*); $\beta = 1035$ (*square*); $\beta = 300$ and 197 (*dot*); Otter [6] $\beta = 61400$ (*crosses*); **e** $\hat{C}_m$ versus K. Same *symbols* as in **d**

particularly the data set from Sarpkaya with $\beta = 1035$ finding good agreement between the simulations and the measurements. Apart from results fitting to the Stokes–Wang solution, we do not find here the same agreement with the results in Sarpkaya and thus neither with Lu et al. An important disagreement is that the present computations conform to the Stokes–Wang solution until separation takes place.

In the flow-separation range we compare the present computed $C_d = 0.36$ to Sarkaya's measured $C_d = 0.5$ for $(\beta, K) = (11240, 4)$, his Fig. 3. We also compare present $C_d = 0.919, 1.1125, 1.335$ for $K = 4.86, 6.28, 8$, respectively, with $\beta = 1035$, to Sarpkaya's measured C_d's in his Fig. 1. It is evident that his C_d-values exceed ours by 40% (i.e., present values multiplied by 1.4 give Sarpkaya's). We note that the inertia coefficients calculated here fit rather well to Sarpkaya's measurements, however.

We note a fundamental difference between U-tube experiments such as those performed by Sarpkaya [5]—oscillating the water while keeping the cylinder fixed, and the experiments by Otter [6]—keeping the water at rest, oscillating the cylinder: it may be speculated if the input oscillatory channel flow gets polluted by turbulence in the former experiments. Present simulations fit well to the experiments by Otter.

We may compare the present computations of the lateral force for $\beta = 11240$ and $K = 4$ to the computations by Lu et al. for $\beta = 1035$ and $K = 3, 5$, their Figs. 3 and 7, respectively. While they find a lateral force up to 16% of F_x for $K = 3$, and up to and even exceeding 50% of F_x for $K = 5$, we find here a rms of F_y of only 2% of F_x. This is another poor comparison between the present LES calculations and those by Lu et al. We note that in the latter computations the original Smagorinsky model was used with the Smagorinsky constant put equal to 0.1, as also used in a lot of similar calculations. However, it is evident from several publications that the dynamic Smagorinsky model quite successfully improves the representation of the turbulent motion which is the case when flow separation occurs; see e.g. [23]. Another difference between our and Lu et al. is that here a finer resolution is employed; presently $1.1–2.2 \times 10^6$ grid cells (runs d–k) compared to Lu et al.'s $0.3–1.5 \times 10^6$ grid cells.

5 Local flow structures

Obtaining the Honji rolls exemplifies the calculation of the local flow structures. The LES calculations at moderate and high K obtain the velocity field during flow separation. There then is strong vortical motion in a large domain surrounding the cylinder. For $K = 4$ this domain extends 9 by 4 diameters along the x- and y-directions, respectively. For $K = 2$ the corresponding extension is 5 by 1 diameters (Fig. 6). The vorticity close to the cylinder is about five times U_m/R (Fig. 7), while in the boundary-layer, the vorticity—the velocity shear—is up to 200 times U_m/R. The boundary-layer thickness in this calculation for $K = 4$, $\beta = 11240$ is $0.01R$ while the grid cell nearest to the wall extends $0.0002R$ radially (Fig. 1b).

During flow separation, the velocity and vorticity fields contain a large range of motion scales which are important to represent accurately. The flow separation involving processes on the small scales has to be computed accurately in order to obtain the force well, where the latter is an example of a global quantity. We exemplify the frequency content of the velocity field by computing the time history of w-velocity in a fixed points $(x, y, z) = (x_0, y_0, z_0)$. The auto-correlation function of $w(t; x_0, y_0, z_0)/U_m$ and its Fourier transform are evaluated as exemplified in Fig. 8. Results are obtained in two points, for $y_0 = 1.02R$ and $y_0 = 3R$ with $(x_0, z_0) = (0, 0)$ is both cases. This clearly show that the energy in the temporal turbulent fluctuations are resolved in the computations.

6 Conclusions

Laminar and LES calculations of the flow and force on an oscillating cylinder in otherwise calm fluid have been performed for β-number ranging from 197 to 61400. The LES code is a modification of CDP, the latter used also for other purposes; it employs the dynamic Smagorinsky model. The computational domain was 30 diameters along the oscillation direction and 10 diameters laterally. The cylinder height H which equals the height of the computational

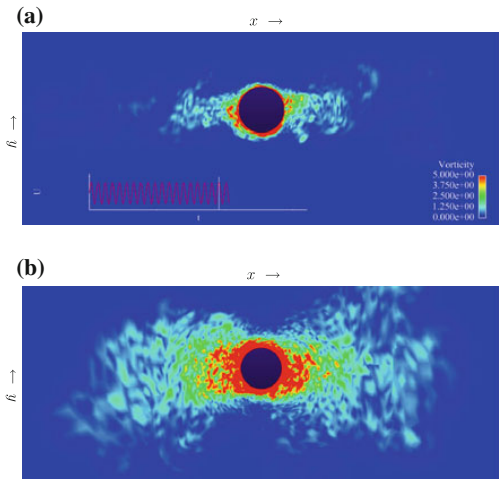

Fig. 6 Vorticity $|\nabla \times \mathbf{v}|/U_\infty/R$. Cut along mid-section $z = 0$. $\beta = 11240$. $KC = 2$ (**a**) and 4 (**b**)

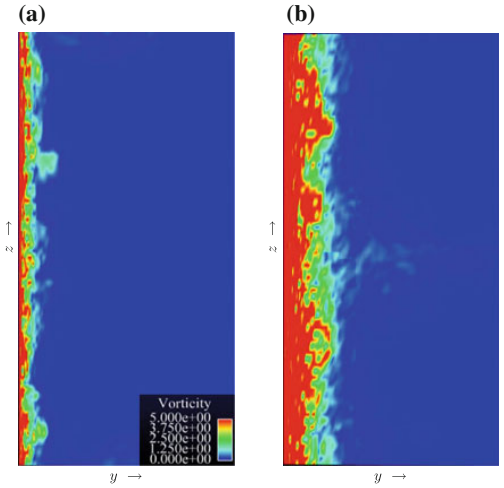

Fig. 7 Same as Fig. 6 but $x = 0$ plane, and $-3R < z < 3R$, $R < y < 4R$

domain was $6R$; in two separate runs H is $8R$ and $4R$. The computational domain extended periodically in all directions.

We have found as main result that the force coefficients follow (or are very close to) the analytical Stokes–Wang solution for Keulegan–Carpenter number K up to 2 where flow separation occurs. The drag coefficient then departs from the Stokes–Wang solution. Our calculations of the force coefficients are in agreement with the experiments by Otter [6]. He obtained the results for $\beta = 61400$ while computations here are performed for a range in β, up to 61400, as indicated above. Present calculations of flow separation, performed for K up to 4 and $\beta = 11240$, with corresponding Re $= 45000$, exhibit a drag coefficient of $C_d = 0.36$, comparing well to the experiments by Otter [6], finding $C_d = 0.31$ for $K = 3.63$ and $\beta = 61400$, and $C_d = 0.44$ for $K = 4.22$ and $\beta = 61400$. Convergence calculations were performed for $K = 4$ and $\beta = 11240$ as well as for the laminar range. Supplementary computations with smaller $\beta = 1035$ and $K = 4.86, 6.28, 8$ (i.e., Re up to 8280) exhibit $C_d = 0.919, 1.1125, 1.335$.

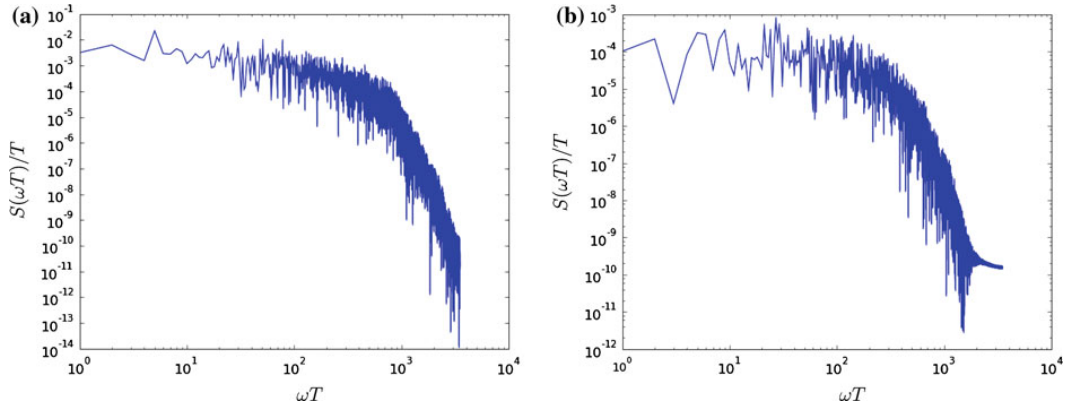

Fig. 8 Temporal spectrum of w-velocity in $(x_0, z_0) = (0, 0)$ and **a** $y_0 = 1.02R$, **b** $y_0 = 3R$

All present drag coefficient calculations are about 40% smaller than C_d's measured by Sarpkaya [5] when flow separation occurs. Inertia coefficients calculated here fit rather well to Sarpkaya's measurements, however.

A surprising result of the laminar calculations is that the force coefficients are the same both before and after the appearance of the Honji instability. They agree with the Stokes–Wang solution (they are 10% higher) but disagree with U-tube experiments obtaining a doubling of the drag coefficient as compared to the Stokes–Wang solution. Particularly Sarpkaya [5,8] has pointed to the Honji instability being the cause of this increase in the drag coefficient. In the present calculations with $(\beta, K) = (197, 2.07)$ and $(300, 2)$ it takes some time until the Honji instability becomes present; it grows from small instabilities at the intersection between the cylinder geometry and the (periodic) walls at the top and bottom (of the cylinder). The instability then grows along the cylinder side, and becomes fully developed after a number of 14 periods, in the present calculations. Wavelength, height and width of the mushroom-shaped streak patterns induced by the Honji rolls fit well to the original experiments [3]. The periodic appearance and disappearance of the rolls are visualized. Fine and moderate grid resolutions show the same streak pattern.

Several experimental sets at high β and K below Hall's stability limit exhibit drag coefficients corresponding to the Stokes–Wang solution. These include [6] and one of the data sets by Johanning [28]. The same has been found in an unpublished experimental data set for $\beta = 20000$ (JR Chaplin (2010), personal communication), and also in other computational attempts than those presented here (JR Chaplin (2010), personal communication). However, Otter's experiments [6] conform also to the Stokes–Wang solution well beyond the stability limit, up to where flow separation occurs, at $K = 2$. These experiments—physical and numerical—conform with the present calculations. Other experimental sets at high β and below the stability limit [7,8,28–30] show drag coefficients twice the Stokes–Wang solution; see the summary by Chaplin and Mouazé's [10]. We note that a problem with the (physical) U-tube experiments, where the cylinder is fixed and the water oscillating, is that the input flow may become polluted by boundary-layer effects and turbulence. The scatter in C_d at high values of β and small K remains an experimental and computational challenge.

Calculations of the Honji rolls exemplify the local flow structures. The present calculations show that the pattern has no consequence for the force on the cylinder, however. The LES calculations of flow separation and vortical flow resolve the flow physics at small scale. The calculations exhibit velocity and vorticity fields containing a large range of motion scales. Evaluation of the frequency contents of the velocity field shows that the energy of the temporal turbulent fluctuations (in fixed points) is resolved in the computations. It is evidenced that the flow separation occurring for $K > 2$ has strong implication for the force on the cylinder. An accurate numerical representation of the flow physics during the separation is needed in order to accurately calculate the force. This implies a relevant modeling of the scales of the flow separation process, that also is three-dimensional.

The finest grid used had a number of 2.2×10^6 cells; it had a finest radial $\Delta r/R = 0.0002$, number of points along the cylinder circumference of 180, $\Delta z/R = 0.044$ and time step of $0.0005T$, for the case $K = 4$, $\beta = 11240$. The simulations presented here were carried out on a computer with 16 cores operating at 2.13 GHz. The simulation time for each case was of the order of 1 week.

Acknowledgements This paper is presented in memory of Professor E. O. Tuck who, with his brilliant analytical approach to a large variety of problems, particularly has inspired the international environments of Applied Mathematics and Hydrodynamics. This research was funded by the Research Council of Norway through NFR 191204/V30.

Appendix: The dynamic Smagorinsky model

In this section we describe how the dynamic Smagorinsky model (DSM) is implemented in the present numerical code. The theoretical descriptions of the DSM is given in e.g. [19,20] and [22].

As our starting point for the description of the dynamic Smagorinsky model we consider the plain Smagorinsky model in which the deviatoric part of the residual stress tensor is approximated by

$$t_{ij}^r = -2c_S\overline{\Delta}^2\overline{S}\,\overline{S}_{ij}, \tag{8}$$

where $\overline{\Delta}$ is the filterwidth $\overline{S} = (2\overline{S}_{ij}\overline{S}_{ij})^{1/2}$ is the characteristic rate of strain, $\overline{S}_{ij}$ is the filtered rate of strain and c_S is the square of the Smagorinsky constant. In the Smagorinsky model c_S is, as the name implies, a constant, e.g. in the work of Lu et al. [11] the Smagorinsky constant is put equal to 0.1, as also used in a lot of similar calculations. In general, however, we must expect that this is not the case; c_S must be viewed as a function of both space and time.

The main idea of the DSM is to apply a second (test) filter, of width $\hat{\Delta}$, to extract the information about the spatial variability of c_S. Usually $\hat{\Delta} \simeq 2\overline{\Delta}$. Applying the test filter to the filtered N–S equations results in a similar equation, but with a different residual stress expression,

$$T_{ij} = \widehat{\overline{U_i U_j}} - \hat{\overline{U}}_i\,\hat{\overline{U}}_j, \tag{9}$$

We approximate the deviatoric part of T_{ij} in the Smagorinsky manner so that we get,

$$T_{ij}^r = -2c_S\hat{\overline{\Delta}}^2\hat{\overline{S}}\,\hat{\overline{S}}_{ij}, \tag{10}$$

If we now consider the difference between (10) and the test filtered (8) we obtain the following if we, quite inconsistently, assume c_S to be uniform [22],

$$L_{ij}^S = T_{ij}^r - \widehat{t_{ij}^r} = c_S\left(2\overline{\Delta}^2\widehat{\overline{S}\,\overline{S}_{ij}} - 2\hat{\overline{\Delta}}^2\hat{\overline{S}}\,\hat{\overline{S}}_{ij}\right) = c_S M_{ij}. \tag{11}$$

Here L_{ij}^S is an approximation to the deviatoric part of the Leonard stresses, where the Leonard stresses are the difference between the two residual stress tensors,

$$L_{ij} = T_{ij} - \widehat{t_{ij}} = \widehat{\overline{U_i}\,\overline{U_j}} - \hat{\overline{U}}_i\,\hat{\overline{U}}_j. \tag{12}$$

As we can see the terms in (12) are known in terms of the filtered velocities and can thus be computed. This means that we can calculate a value of c_S that minimizes the difference between L_{ij}^S and the deviatoric part of L_{ij}. This is done by minimizing the mean-square error [20] according to,

$$c_S = \frac{M_{ij}L_{ij}}{M_{kl}M_{kl}}. \tag{13}$$

In the present numerical code the eddy viscosity $\nu_T = c_S \overline{\Delta}^2 \overline{S}$ is computed using the filtered velocity field from the previous timestep. The coefficient c_S is computed according to

$$c_S \overline{\Delta}^2 = \frac{\widehat{M_{ij} L_{ij}}}{\widehat{M_{kl} M_{kl}}}, \tag{14}$$

where L_{ij} is as given above. In this particular application M_{ij} is modified into

$$M_{ij} = 2 \left(\widehat{\overline{S}\, \overline{S}_{ij}} - \hat{\overline{\Delta}}^2 / \overline{\Delta}^2 \hat{\overline{S}}\, \hat{\overline{S}}_{ij} \right). \tag{15}$$

The local averaging obtained by the filtering in (14) is necessary for stability [19]. As an additional stabilising step all negative values of eddy viscosity are set to zero.

Finally, to complete the description of the model the filters and their widths need to be specified. For the $\overline{\Delta}$ width filter the filtering is implicit and the filterwidth is taken to be proportional to the mesh spacing, i.e., $\overline{\Delta} = (V)^{1/3}$, where V is the control volume. The $\hat{\Delta}$ filter is a weighted average of the value at the node and its neighbours. The filter width ratio is taken to be $\hat{\overline{\Delta}}/\overline{\Delta} = \sqrt{6}$.

References

1. Stokes GG (1851) On the effect of the internal friction of fluids on the motion of pendulums. Trans Camb Philos Soc 9:8–106
2. Wang C-Y (1968) On high-frequency oscillatory viscous flows. J Fluid Mech 32:55–68
3. Honji H (1981) Streaked flow around an oscillating circular cylinder. J Fluid Mech 107:509–520
4. Hall P (1984) On the stability of the unsteady boundary layer on a cylinder oscillating transversely in a viscous fluid. J Fluid Mech 146:347–367
5. Sarpkaya T (1986) Force on a circular cylinder in viscous oscillatory flow at low Keulegan-Carpenter numbers. J Fluid Mech 165:61–71
6. Otter A (1990) Damping forces on a cylinder oscillating in a viscous fluid. Appl Ocean Res 12:153–155
7. Chaplin JR (2000) Hydrodynamic damping of a cylinder at $\beta \approx 10^6$. J Fluids Struct 14:1101–1117
8. Sarpkaya T (2001) Hydrodynamic damping and quasi-coherent structures at large Stokes numbers. J Fluids Struct 15:909–928
9. Johanning L, Bearman PW, Graham JMR (2001) Hydrodynamic damping of a large scale surface piercing circular cylinder in planar oscillatory motion. J Fluids Struct 15:891–908
10. Chaplin JR, Mouazé D (2004) Disturbed laminar flow over an oscillating cylinder. In: XXI international congress on theoretical and applied mechanics, 15–21 Aug 2004, Warsaw, Poland. http://fluid.ippt.gov.pl/ictam04/CD_ICTAM04/FSM4/12557/FSM4_12557.pdf
11. Lu X, Dalton C, Zhang J (1997) Application of large eddy simulation to an oscillating flow past a circular cylinder. J Fluids Eng 119:519–525
12. Lu X-Y, Ling GC (2003) Three-dimensional instability of an oscillating viscous flow past a circular cylinder. Appl Math Mech (English edition) 24:791–800
13. Wu J-Z, Lu X-Y, Zhuang L-X (2007) Integral forces acting on a body due to local flow structures. J Fluid Mech 576:265–286
14. Dütsch H, Durst F, Becker S, Lienhart H (1998) Low-Reynolds-number flow around an oscillating circular cylinder at low Keulegan-Carpenter numbers. J Fluid Mech 360:249–271
15. An H, Cheng L, Zhao M (2010) Direct numerical simulation of oscillatory flow around a circular cylinder at low KC number. J Fluid Mech (in press)
16. Leonard A (1975) Energy cascade in large-eddy simulations of turbulent flows. Adv Geophys 18(1):237–248
17. Smagorinsky J (1963) General circulation experiments with the primitive equations. Mon Weather Rev 91(3):99
18. Lilly DK (1967) The representation of small-scale turbulence in numerical simulation experiments. In: Goldstine HH (ed) Proceedings of IBM scientific computing symposium on environmental sciences. IBM, Yorktown Heights, NY, pp 195–210
19. Germano M, Piomelli U, Moin P, William HC (1991) A dynamic subgrid-scale eddy viscosity model. Phys Fluids A Fluid Dyn 3:1760–1765
20. Lilly DK (1992) A proposed modification of the Germano subgrid-scale closure method. Phys Fluids A Fluid Dyn 4:633–635
21. Meneveau C, Lund TS, Cabot WH (1996) A Lagrangian dynamic subgrid-scale model of turbulence. J Fluid Mech 319:353–385
22. Pope SB (2000) Turbulent flows. Cambridge University Press, Cambridge
23. Pope SB (2004) Ten questions concerning the large-eddy simulation of turbulent flows. New J Phys 6:35. doi:10.1088/1367-2630/6/1/035
24. CITS (2004) Annual technical report. Center for Integrated Turbulence Simulations, Stanford. http://www.stanford.edu/group/cits/pdf/reports/cits2004.pdf

25. CITS (2005) Annual technical report. Center for Integrated Turbulence Simulations, Stanford. http://www.stanford.edu/group/cits/pdf/reports/cits2005.pdf
26. Ham F, Iaccarino G (2004) Energy conservation in collocated discretization schemes on unstructured meshes. Centre for Turbulence Research, Stanford. http://ctr.stanford.edu/ResBriefs04/ham_iaccarino.pdf
27. Ham F, Mattasson K, Iaccarino G (2006) Accurate and stable finite volume operators for unstructured flow solvers. Centre for Turbulence Research, Stanford. Annual Research Briefs. http://ctr.stanford.edu/ResBriefs06/19_ham1.pdf
28. Johanning L (2003) PhD thesis. Imperial College, London
29. Bearman PW, Russel MP (1996) Measurements of hydrodynamic damping of bluff bodies with application to the prediction of viscous damping of TLP hulls. In: 21st symposium on naval hydrodynamics, Trondheim, Norway, pp 61–73
30. Chaplin JR, Subbiah K (1998) Hydrodynamic damping of a cylinder in still water and in a transverse current. Appl Ocean Res 20:251–259

Errata

Farah Rashid, Magnus Vartdal and John Grue[1]: Oscillating cylinder in viscous fluid: calculation of flow patterns and forces. J. Eng. Math. (2011) 70:281-295, DOI 10.1007/s10665-010-9395-7

[1]e-mail: johng@math.uio.no

We have found an error in the script calculating the drag coefficient, in this publication. This affects the drag coefficients obtained in table 2, on p. 285, which, correctly evaluated become about 20 percent higher than what we have published. The mass coefficients are unchanged. The main conclusions of the paper remain. The correct table 2 is given below (see the paper for definition of symbols).

Table 2. Force coefficients for different values of β and K

run	β	K	$\hat{C}_m$	$(\hat{C}_m + 1)/\mathrm{W}$	C_d	C_d/W
a	300	2.0	1.108	0.989	0.981	1.254
b 1,2	197	2.07	1.135	0.989	1.170	1.245
d	1035	2.5	1.017	0.975	0.638	1.920
e	1035	4.86	0.856	0.896	1.032	6.055
f	1035	6.28	0.780	0.844	1.277	9.667
g	1035	8.0	0.566	0.753	1.538	14.85
h	11240	1.0	1.025	1.002	0.258	1.035
i	11240	2.0	1.013	0.996	0.206	1.657
j 1,2,3	11240	4.0	0.950	0.970	0.444	7.132
k	61400	0.5	1.016	1.003	0.209	0.984

PART II

Laboratory modelling of breaking internal solitary waves

James P Franklin[1], Stuart E King[2], Magda Carr[2], Peter A Davies[1], John Grue[3], Daniela Laskovski[3], Farah Rashid[3], Yakun Guo[4], David G Dritschel[2].

[1]Department of Civil Engineering, The University, Dundee DD1 4HN, UK
[2] School of Mathematics & Statistics, University of St Andrews, Mathematical Institute, St Andrews KY16 9SS, UK
[3]Department of Mathematics, University of Oslo, P.O. Box 1053 Blindern, 0316, Norway
[4] School of Engineering, University of Aberdeen, King's College, Aberdeen AB24 3UE, UK
p.a.davies@dundee.ac.uk

Abstract

Results are presented from laboratory experiments conducted to investigate shear-induced breaking of internal solitary waves in shallow, 3-layer, stably-stratified fluid systems. The development of the breaking process for unstable waves has been studied over a wide parameter range, with particular emphasis on the temporal and spatial structure and evolution of the billows generated in the breaking process. Data derived from quasi-instantaneous density profiles through the billows are presented, to determine the density perturbation fields within a given billow and at different stages of billow development. Estimates of Thorpe length scales L_T and billow height L_B have been derived to quantify the internal structure of the billows and it is demonstrated that the relationship between these length scales does not differ significantly from the corresponding relationship for shear induced billows in uniform shear flows.

1. Introduction

Internal solitary waves (ISWs) propagate on density interfaces in stably-stratified fluids and, in a geophysical context, they are observed throughout the Earth's oceans and atmosphere. In the ocean they are generated primarily by barotropic tidal flow over uneven bottom topography (Farmer and Armi, 1999; Apel, 2002, Vlasenko *et al*., 2005) and they travel as rank-ordered (in amplitude) packets. Oceanic internal solitary waves/solitons have attracted significant scientific interest since technological advances in synthetic aperture radar (SAR) imagery revealed the existence of such waves in most of the Earth's shelf seas and even in the deep oceans (Apel, 2002). Ship-based observations have shown that the waves may reach amplitudes comparable with the water column depth; see, for example, Duda *et al* (2004) who report ISWs of depression of amplitude 150 m in a water depth of 340 m and Van Gastel *et al* (2009) who measured a maximum vertical isopycnal displacement of 83 m in a total water depth of 124 m. They may be waves of depression (see above) or waves of elevation (*e.g*. Moum *et al*., 2007), depending upon whether the pycnocline is respectively above or below the mid-depth of the water column. Interest is focussed here on the former type. The recent comprehensive review by Helfrich and Melville (2006) provides a convenient entry point into the ISW literature.

ISWs are known to break as a result of either convective or shear-driven instability (or a combination of both), but the condition for shear-induced breaking (the case of interest here) has been obtained only recently[1]. Grue at al (1999) reported the first laboratory experiment to document breaking in ISWs for Ri_{min} = 0.07, while noting that for Ri_{min} = 0.23 the wave

[1] Field observations showing breaking oceanic ISWs are reported by Moum *et al* (2003).

was stable. (Here Ri is the local Richardson number, defined conveniently (Fructus and Grue, 2004) as $Ri = c(c - u)/\delta^2 N_\infty^2$, where c is the wave speed, u is the horizontal velocity, δ the vertical excursion of the streamline relative to rest in the steady frame of reference of the wave and N_∞ is the value of the buoyancy frequency in the far-field (obtained by tracing along a streamline in the steady-state)). Laboratory and numerical investigations (Fructus *et al*, 2009) in 3-layer stratified systems consisting of two homogeneous layers separated by a linearly stratified pycnocline have demonstrated subsequently that breaking occurs through shear instability when the horizontal width L_x of the pocket defined by Ri <1/4 in the wave core exceeds 0.86 times the wave width λ at half amplitude – a condition verified subsequently by Barad and Fringer (2010) and Lamb and Farmer (2011). Most significantly, the theoretical analyses demonstrate that large amplitude ISWs may remain stable for values of the local Richardson number Ri much less than ¼, a finding in agreement with field observations (Duda *et al*., 2004) and modelling studies of periodic internal waves (Troy and Koseff, 2005).

The breaking of ISWs due to shear instability is characterised by the formation of a sequence of rolled vortices (billows). Each of the billows grows with time until arrested by the stratification within the pycnocline, before breaking down to form a turbulent patch. In this regard the behaviour resembles qualitatively that associated with the classic Kelvin-Helmholtz (K-H) instability of the interface between two fluids in parallel motion with different velocities and densities (see, for example, de Silva *et al*., 1996; Strang and Fernando, 2001). Note, however, that the temporal and spatial development of the billows in the case of breaking ISWs is *a priori* affected significantly by the horizontal non-uniformity in velocity within each of the constituent layers. The purpose of the present paper is to describe measurements of the development of the density field within a breaking ISW billow. In particular, data are presented on the Thorpe scale L_T - a measure of the length scale of turbulent overturning events within the billow (Dillon, 1982; Thorpe, 2005) – and the vertical extent L_B of the billow throughout the growth and decay process.

2. Laboratory Modelling

2.1 Experimental arrangement.

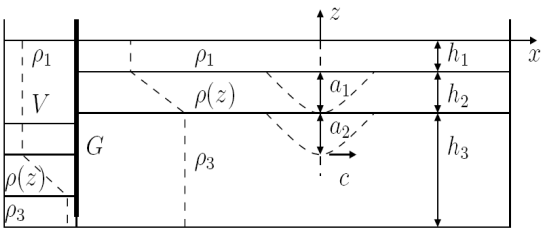

Figure 1: Schematic view of the laboratory model configuration – see text for definition of symbols

The laboratory configuration and method of ISW generation is illustrated schematically on Figure 1. A rectangular-section, horizontal tank is filled initially with a layer of brine solution of density ρ_3 and thickness h_3. A linearly-stratified layer of thickness h_2 is then placed above the brine layer using the conventional double reservoir technique, such that, within this layer (the pycnocline) the density varies between ρ_3 and ρ_1, the density of the fresh water layer of thickness h_1 added above the pycnocline. A solid gate G placed close to one end of the tank is then partially-lowered and an excess volume V of fresh water of density ρ_1 added behind the

gate, as shown. The addition of the excess volume depresses the pycnocline behind the gate such that, when the gate is removed vertically, an internal solitary wave propagates with celerity c along the interface in the main part of the channel. The geometrical dimensions of the section of the tank behind the gate (and the magnitude of the excess volume V) are chosen (Kao *et al*., 1985) to generate a single solitary wave.

2.1 Procedure and measurement systems.

Two tanks (with dimensions (12.6 m x 0.5 m x 1.0 m) and (6.4 m x 0.4 m x 0.6 m) respectively) were utilised in the experimental programme. Each was constructed from transparent glass panels supported within a steel framework, permitting full observation of the propagating ISWs. A lightbox illuminated a thin z-x section (see Figure 1) at the mid plane of the channel and the motions within this sheet of small, neutrally-buoyant tracer particles added to the fluid were recorded by an array of stationary digital video cameras mounted outside the tank and looking in through the side panels. Using *DigiFlow* software (Dalziel, 2006), particle image velocimetry (PIV) was applied to the digital camera records to derive synoptic velocity and vorticity fields within the illuminated sections; by overlapping the fields of view of the 3 cameras, it was possible to record and follow simultaneously the behaviour of the wave over at least one full wavelength.

Density profile data were acquired along the mid-plane of the tank by means of an array of 12 fast-response, four-electrode, micro-conductivity probes (Head, 1983) mounted together above the tank frame on a computer-controlled, motorised rack and pinion traverse system. The traverse was controlled to simultaneously drive all probes vertically through the fluid at a speed of about 10 $cm.s^{-1}$ when the aft portion of the wave came within the measurement section. By suitable trial and error it was possible to synchronise the motion of the traverse with the arrival of the aft portion of the wave so that at least 1 probe (and usually 3-4) penetrated the centres of individual billows formed by wave breaking. The composite image in Figure 2 illustrates the approach of the breaking ISW to the probe assembly.

Figure 2: Composite image (side view) of breaking internal solitary wave approaching probe assembly (top right)

2.1 Results

Figure 3 shows a time sequence of false-colour images illustrating the occurrence, growth and decay of a typical billow in a sequence of typically 5-6 identifiable billows (see Figure 1) in the breaking portion of the ISW. The initial perturbation (Figure 3(i)) is seen to grow with time and develop a characteristic overturning form (Figure 3 (iv)) until a recognisable cat's eye-type, closed billow is formed (Figure 3(v)). The onset of significant mixing within the billow is indicated by the appearance of blurring in the image (Figures 3(vi), (vii)) caused by refractive index differences associated with the brine and freshwater layers. The temporal

growth in the vertical extent of an individual billow is also evident from Figure 3, though the size of the feature is difficult to determine accurately from visual observation when the mixing process starts (Figure 3(vii)).

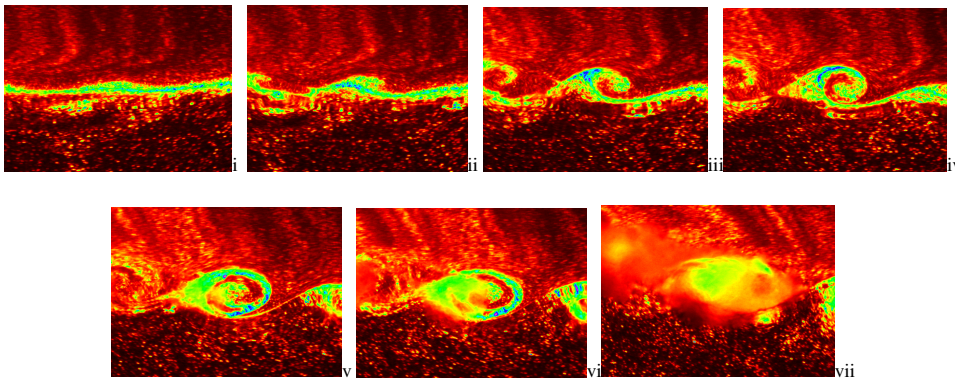

Figure 3: Sequence of frames showing time development of a single interfacial billow for a breaking internal solitary wave. Direction of wave propagation from Left to Right

The growth phase can be seen by considering the full spatial sequence of billows (see Figure 4) in the breaking portion of the wave, where each of the constituent billows may be regarding as representing different stages of development of an individual billow. It is important to note that the velocity shear across the interface decreases with horizontal distance (x) from the maximum depression point of the wave (see, for example, Fructus and Grue, 2004) so the environment in which an individual billow develops will vary with elapsed time.

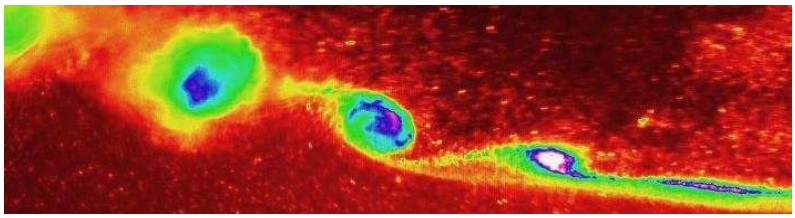

Figure 4: Image showing the spatial development of a sequence of billows in the breaking portion of an internal solitary wave. Direction of wave propagation from Left to Right.

Figure 5 shows an instantaneous image of the probes as they pass simultaneously through the billow sequence, together with an instantaneous density profile recorded by one of the probes that has passed through an individual billow that has reached the cats-eye stage of development. The distortion of the linearly stratified region in the core of the billow is seen clearly in the profile, together with a characteristic signal (namely the appearance in the profile of anomalously high and low density regions at the upper and lower extremities) of the overturning motion at the edges of the billow.

As indicated above, the distorted density profiles taken through the billows can be processed to provide values of the Thorpe scale L_T and the vertical extent (local billow height) L_B of the billow. (The quantity L_B may also be measured directly from the video record by identifying

appropriate pixel values in a consistent and objective manner). The procedure followed here for deriving the Thorpe scale L_T has been described extensively elsewhere in the literature (*e.g*. Dillon, 1982; de Silva *et al*., 1996). It consists of (i) sorting the measured profile data to generate the statically-stable state of minimum potential energy, (ii) calculating the vertical distances l_d (the Thorpe displacements) each fluid parcel has to be moved to achieve this sorted (monotonised) profile and (iii) determining L_T as the r.m.s value of all of the individual l_d values within the billow.

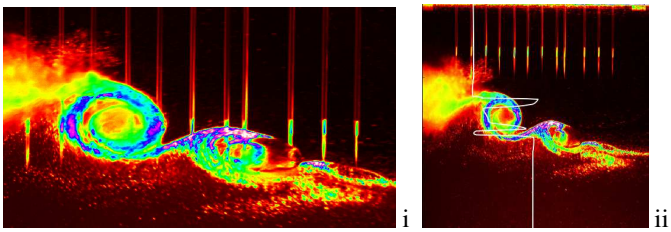

Figure 5: Close up showing (i) penetration of 3 billows by the micro-conductivity probe array and (ii) instantaneous overlaid density profile from probe 4 (from left)

Figure 6 shows a composite, dimensional plot of L_B versus elapsed time t for 3 different billows (see Figures 2 and 4) tracked during a single experiment. The temporal growth of the billows in the vertical direction, illustrated clearly in Figure 3, is shown (at least in this case) to consist of a monotonic increase, with a growth rate that decreases with time. The plot resembles closely the temporal growth of K-H billows for stratified shear flows with uniform parallel layers (de Silva *et al*., 1996). Note, in particular, that the maximum value of L_B reached during the experiment of Figure 6 is much less (a factor of about 4) than the scale $(\Delta U)^2/g_0'$ representing the maximum billow height for the configuration studied by de Silva *et al* (1996) where ΔU represents the velocity difference across the flowing layers of densities ρ_3 and ρ_1, g is the acceleration due to gravity and $g' = (\rho_3 - \rho_1)/\rho_1$ is the modified gravitational acceleration associated with the rest configuration. (Application of this scale to the breaking ISW cases requires the specification of a reference velocity difference ΔU, not only because this velocity scale is an internal property of the flow but also because it varies with distance $\pm x$ from the maximum depression location of the wave. For comparison purposes, the maximum value of ΔU, measured at the maximum depression location, was used).

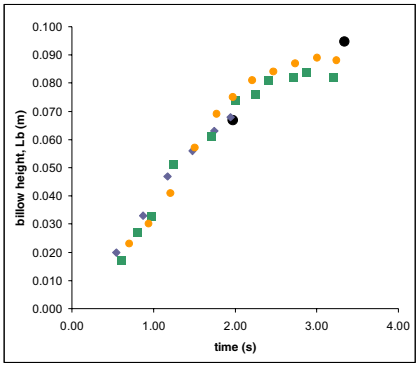

Figure 6: Dimensional plot of variation of billow height L_B versus elapsed time t for 3 different billows (video record measurements depicted as ■,♦,●, with complementary direct probe strike data (●))

The composite plot in Figure 7 shows the relationship between L_B and L_T for all of the breaking ISW experiments conducted. The plot shows that, regardless of scatter and the amalgamation of data from different external conditions, the relationship between L_B and L_T is well represented by a linear relationship with a coefficient of 0.38 linking the two dimensions. This value may be compared with that (0.49 ± 0.03) obtained by de Silva *et al* (1996) for the reference case of a stratified shear flow with uniform parallel layers.

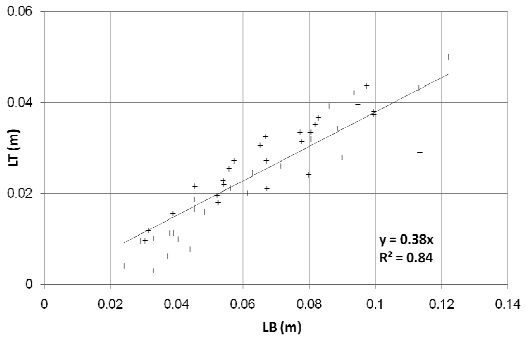

Figure 7: Dimensional composite plot (all experiments) of variation of L_T versus L_B , with best-fit linear regression.

3. Numerical Modelling

Though the focus of the present paper is the laboratory modelling of ISWs, recent studies by the authors (King *et al*., 2010; Carr *et al*., 2011) have developed numerical models employing a combination of contour advection and pseudo-spectral techniques (Dritschel & Ambaum, 1997; Dritschel & Fontane, 2010) to simulate shear-induced breaking of ISWs for steady and unsteady Boussinesq cases respectively. The numerical model illustrates (see Figure 8) that billows form near the trough of the wave, subsequently growing and disturbing the tail.

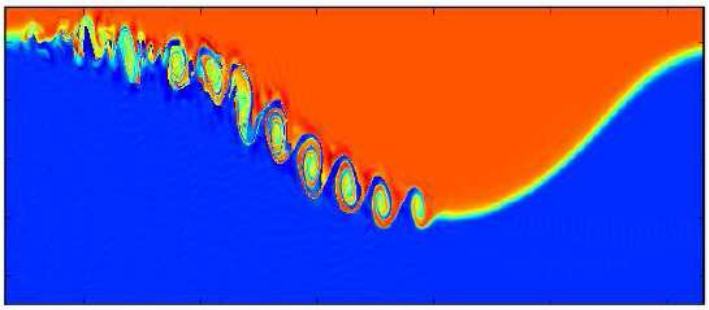

Figure 8: Numerical simulation of shear-induced instability and billow formation in an internal solitary wave propagating in a 3-layer stably-stratified fluid.

Furthermore, computations of the density field within a growing billow (see Figures 9(i),(ii)) enable predictions to be made of L_B and L_T and the variation of these quantities with distance from the centre of the billow (Figure 9(iii).

3. Summary and conclusions

Laboratory experiments on internal solitary waves in a 3-layer, stably-stratified fluid have demonstrated the breaking of such waves by shear instability and the consequent formation of a sequence of billows in the aft portion of the wave. The measured temporal and spatial development of individual billows in the sequence reveal that the principal features, namely the initial development of a characteristic cat's eye pattern followed by a growth in vertical extent and an eventual collapse into an isolated mixed turbulent patch, resemble qualitatively

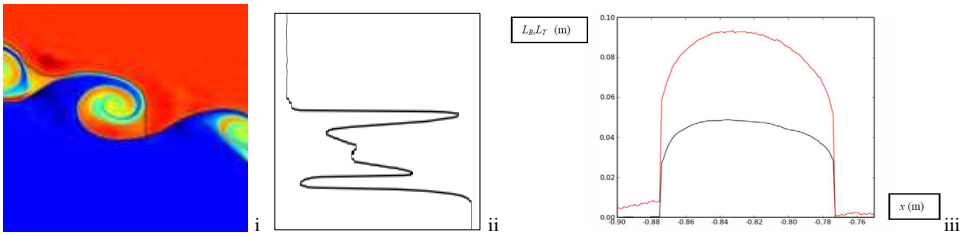

Figure 9: Numerical modelling of (i) billow growth, (ii) instantaneous density field within growing billow and (iii) corresponding computations of variation of L_B and L_T with x within the billow.

the development of K-H billows for uniform stratified shear flows and periodic internal waves. Measurements show that the Thorpe (L_T) and height (L_B) scales of the billows can be represented well by a linear relationship with a proportionality coefficient of 0.38, a value that is less than (but of the same order as) the corresponding value predicted by a numerical model. Further studies to scale the dimensions and the temporal growth/decay of the billows in terms of the external parameters are in progress.

Acknowledgements

The study was supported by the UK Engineering & Physical Sciences Research Council, the Northern Research Partnership, The Norwegian Research Council and the Universities of Dundee and Oslo.

References

Apel, J. R. (2002). Oceanic internal waves and solitons. In ***An Atlas of Oceanic Internal Solitary Waves***, Global Ocean Associates, Washington DC, USA (prepared for the Office of Naval Research (322 PO).

Barad, M.F. and Fringer, O.B. (2010) Simulations of shear instabilities in interfacial gravity waves. *J. Fluid Mech.*, 644:61-95

Carr, M., King, S.E., and Dritschel, D. G. (2011) Numerical simulation of shear-induced instabilities in internal solitary waves. *J. Fluid Mech.*, (in press)

De Silva, I.P.D., Fernando, H.J.S., Eaton, F. and Hebert, D. (1996) Evolution of Kelvin-Helmholtz billows in nature and laboratory. *Earth & Planet. Sci. Letters*, 143:217-231.

Dillon, T.M. (1982) Vertical overturns: a comparison of Thorpe and Ozmidov length scales. *J. Geophys. Res.*, 87(C12):9601-9613.

Dritschel, D. G., and Ambaum, M. H. P. (1997) A contour-advective semi-Lagrangian numerical algorithm for simulating fine-scale conservative dynamical fields. *Quart. J. R. Met. Soc*., 123: 1097–1130.

Dritschel, D. G., and Fontane, J. (2010) The combined Lagrangian advection method. *J. Comput. Phys*., 229: 5408–5417.

Duda, T.F., Lynch, J.F., Beardsley, R.C., Ramp, S.R., Chiu, C.S., Tang, T.Y. and Yang, Y J. (2004) Internal tide and non-linear internal wave behavior at the continental slope in the northern South China Sea. *IEEE J. Oceanic Engineering*, 29 (2004): 1105-1130

Farmer, D. M. & Armi, L. (1999) The generation and trapping of solitary waves over topography. *Science* 283: 188-190.

Fructus, D. and Grue, J. (2004) Fully nonlinear solitary waves in a layered stratified fluid. *J. Fluid Mech*., 505:323-347.

Fructus, D., Carr, M., Grue, J., Jensen, A. and Davies, P.A. (2009) Shear induced breaking of large internal solitary waves. *J. Fluid Mech*., 620:1-29

Grue, J., Jensen, A., Rusås, P-O. and Sveen, J.K. (1999) Breaking and broadening of internal solitary waves. *J. Fluid Mech*., 413:181-217.

Head, M. J. (1983) The use of miniature four-electrode conductivity probes for high resolution measurement of turbulent density or temperature variations in salt-stratified water flows. Ph.D. Thesis, University of California, San Diego, USA.

Helfrich, K.R, and Melville, W.K. (2006) Long nonlinear internal waves. *Ann. Rev. Fluid Mech*., 38:395-425.

Kao, T.W., Pan, F-S. and Renouard, D (1985) Internal solitons on the pycnocline: generation, propagation and shoaling and breaking over a slope. *J. Fluid Mech*., 159:19-53

King, S. E., Carr, M., and Dritschel, D. G. (2010) The steady state form of large amplitude internal solitary waves. *J. Fluid Mech*., 666: 477–505.

Lamb, K. G., and Farmer, D.M. (2011) Instabilities in an internal solitary-type wave on the Oregon shelf. *J. Phys. Oceanogr*., 41:67-87

Moum, J.N., Farmer, D.M., Smyth, W.D., Armi, L. and Vagle, S. (2003) Structure and generation of turbulence at interfaces strained by internal solitary waves propagating shore-ward over the continental shelf. *J. Phys. Oceanogr*., 33: 2093–2112.

Moum, J.N., Klymak, J.M., Nash, J.D., Perlin, A. and Smyth, W.D. (2007) Energy transport by non-linear internal waves. *J. Phys.Oceanogr*., 37:1968-1988.

Strang, E.J. and Fernando, H.J.S. (2001) Entrainment and mixing in stratified shear flows. *J. Fluid Mech*., 428:349-386.

Thorpe, S.A. (2005) ***The Turbulent Ocean***. Cambridge University Press, Cambridge, UK

Troy, C. D. and Koseff, J.R. (2005) The instability and breaking of long internal waves. *J. Fluid Mech*., 543:107-136

Van Gastel, P, Ivey, G. N., Meuleners, M.J., Antenucci, J.P. and Fringer, O. (2009) The variability of the large-amplitude internal wave field on the Australian North West Shelf. *Continental Shelf Res*., 29: 1373-1383.

Vlasenko, V., Stashchuk, N. and Hutter, K. (2005) ***Baroclinic Tides: Theoretical Models and Observational Evidence***, Cambridge University Press, Cambridge, UK.

PART III

APPENDIX

Appendix

Experimental Study and Image Velocimetry

1 Introduction

The current study of internal waves in this thesis is based on experimental work. Studies based on laboratory work have a significant role in research. Experimental studies can be employed to verify analytical solutions and can also be used to check the validity of numerical simulations. Experimental studies have helped to understand the internal wave phenomenon at large scales in the ocean, and the mechanisms of wave generation, propagation, circulation, dissipation, evolution etc. Large scale studies have contributed towards the explanation of the features and associated properties of the internal waves. This includes work by Farmer & Smith (1980); Apel *et al.* (1985), they studied internal waves which are generated by tidal flows on release of large bodies of salt and fresh water, flowing from one part of ocean to the other. Field studies done by Duda *et al.* (2004) and Ramp *et al.* (2004) recorded internal wave data at the continental slope in the Northern South China Sea. Their study is a combination of moored and ship board observations. They described in detail the internal waves as they propagate along the continental slope.

Internal waves have been studied mathematically, experimentally and numerically, and results of these different modes of studies have also been compared with the field studies. The studies based on laboratory work play a strong role to interpret observations on large scale. For example Wallace & Wilkinson (1988) and Helfrich (1992), in their experimental observations showed internal wave run-up on slope and breaking of waves with the formation of boluses. Lamb (1994) numerically investigated nonlinear evolution of the internal wave field generated by tidal flow across a bank edge. He motivated his study by the complex internal wave phenomenon observed on Georges Bank. Experimental research by Grue *et al.* (1999) compared the experiments with a fully nonlinear interface model and weakly nonlinear Korteweg-de Vries (KdV) theory. Cai *et al.* (2003) investigated the forces and torques exerted by internal soliton on cylindrical pile. In their study they employed Morison's method and introduced separation and regression analysis to estimate the forces on piles. They also recorded a set of observational data near Dongsha Islands in the northern South China Sea.

A major achievement towards the understanding and visualisation of the large scale studies was made after the formation of flow visualisation techniques were introduced.

Previously, the experimental tools were restricted to qualitative statements, these flow visualisation techniques are now employed carefully in experimental studies at small scale to make observations and extract results. After the pioneering work by Ludwing Prandtl, Raffel *et al.* (2007) the scientific and technical progress in optics, laser and computer techniques has made it possible to further develop and enhance the flow visualization techniques such that the quantitative measurements can be extracted from the complex flow problems as well.

In the laboratory studies of flow measurement, various techniques have been used to measure and record the flow. These techniques include resistance wave guages, hot-film probes or Laser Doppler velocimetry, Hot-wire anemometry etc. In Raffel *et al.* (2007), particle image velocimetery has been discussed in detail in variety of flow problems. They have discussed in detail the arrangements required for experiments and techniques of extracting data out of the experiments. They have also described the physical and technical background required for the better understanding of these techniques. These techniques were successfully used in several experimental studies. Grue (2004) in his detailed analysis and description has described laboratory measurements of internal waves using Particle Image Velocimetry and Particle Tracking Velocimetry. He also reviewed various studies of internal waves done by PIV and PTV. Sveen & Cowen (2004) provided a detailed overview of quantitaive imaging techniques (QI). They discussed in detail the QI methods and their accuracy. They also discussed QI techniques as a digital data analysis with software that is based on principles of pattern matching. Umeyama (2008) reviewed transformation processes and nonlinear properties of internal waves over a uniform slope using PIV techniques.

The current set of experimental studies Particle Image Velocimetery (PIV) and Particle Tracking Velocimetery (PTV) have been used to process the recorded data. The main difference between these techniques and PIV is that PIV can produce two dimensional or even three dimensional vector fields, while the other techniques measure the velocity at a point. PIV and PTV are both powerful experimental methods to extract the velocity field and related dynamics of the waves observed in the tank. PIV is a technique which allows the velocity of a fluid to be simultaneously measured throughout an illuminated section, which is commonly a plane. Whereas, in the PTV method individual particles

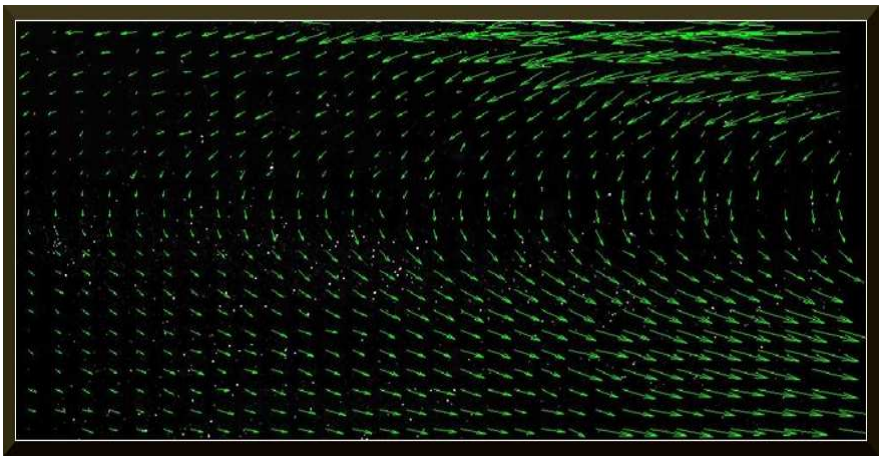

Figure 1: Velocity field of the wave at FoV-I with initial volume 25 litres

are traced in sequence of images.

The objective of this document is to present the technical features of the PIV system employed in the Hydrodynamics Laboratory, Department of Mathematics, University of Oslo. Experimental setup was designed for the study of internal waves in two wave tanks. For the recording and observation of wave propagation and breaking the tank used had dimensions (12.6 m x 0.5 m x 1.0m). For the study of internal waves propagating along the slope the tank was 7m long and 0.25m wide. Fields of view were marked to make the measurements. For the implementation of PIV and PTV, these FoVs were illuminated by ordinary white light for the recording of wave breaking. While for the recording of wave propagation along the slope, the recording sections were illuminated by laser light. The fields of view had a width of about 5mm. Flow-following particles were introduced into the flow and their motion was used to estimate the kinematics of the local fluid.

Effort has been made to describe the data acquisition procedure and the setup established in the lab. Components of PIV are presented and the processing of the data is also discussed.

2 Data Acquisition

The current PIV data acquisition setup comprised of high speed digital cameras and the light source to enlight the area of interest. To enlighten the flow in the area of interest, white light source in part 2 of the experimental study was placed under the tank. Pulsed laser in the experimental setup of part 3 of this thesis was employed. The viewing illuminated section which is the area of interest is referred to as field of view (FOV)

2.0.1 The Laser

The recording sections of the tank were illuminated by ND:YAG laser. ND:YAG laser is a standard light source for recent PIV systems. Its high pulse energy, short pulse duration and adjustable time interval makes its ideal for particle imaging. The laser component employed in the current study is identified as CFR200 (compact folded resonator) Cabinet ICE (Integerated Cooler and Electronics) from the firma BIG Sky Laser. Distinguishing features of CFR200 include quick lamp change feature, shock and vibration tested and ideal for real world applications. The CFR200 PIV systems are designed to supply two laser pulses in rapid succession.

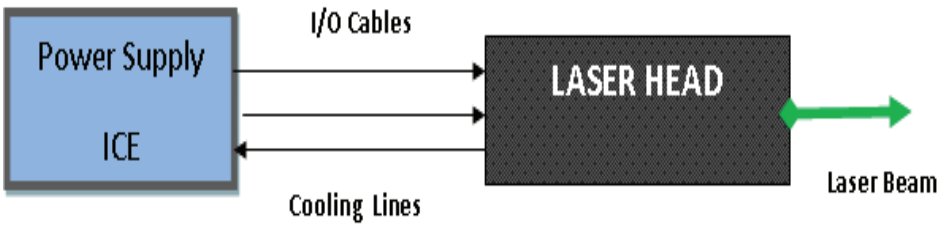

Figure 2: System block diagram of CFR200 Cabinet integrated cooler and electronics laser

The laser system is composed of two main components, ICE and laser head. The main function of ICE is to supply power and cooling to the installation, ND:YAG User Manual v1 (2004). The second component is the laser head. The block diagram of the laser system is shown in figure 2.

Laser generates more heat than ordinary light. The laser uses a closed loop, distilled water cooling system with a liquid-to-air heat exchanger to keep the laser rod and flash-lamp cool. Laser head is composed of electronic assemblies this includes lamp trigger transformer and Q-switch driver. Q-switching is a technique incorporated in the laser by which a laser can be made to produce a pulsed output beam. This technique allows the production of light pulses with extremely high power. And ICE includes all the controls and indicators necessary to operate the system. The key features of ICE are given below.

- provides the power supply to flash pump the laser rod.
- maintains the system timings
- keeps the synchronization

ICE is a single, compact portable unit that carries the Power Supply and Cooler. The ICE front panel has all the functions and displays which are required to manually operate the system. When the system prime power is turned on via the key switch the cooling system is powered up automatically. The system is also provided with the coolant interlocks, their role is to prevent laser operation without coolant flow and during over-temperature conditions.

2.0.2 Operating Features

Neodymium Yttrium Aluminum Garnet lasers (Nd:YAG) have many applications in todays world. A Nd:YAG laser can be operated in a continuous wave (CW) Q-switched or mode-locked methods. A Q-switched laser produces repetitive pulses of tens of nanoseconds duration the same is applied in the current setup. Nd:YAG laser can be optically pumped using lasers of several different wavelengths.

The gain medium is the YAG crystal which is doped with around 1% neodymium by weight. Nd:YAG lasers are four level laser systems i.e. there are four energy levels involved in laser action as shown in figure 3 Davis (2011). The decay rates of these levels are around 230 ns. The advantage of a four level laser system as opposed to a three level laser system is a lower threshold pump power. For the laser system to work, an interaction between photons and the gain medium is required. This interaction involves absorption

or emission of radiation. In the case of absorption, there is an upward transition from a level with energy E_1 to a level with energy E_2 when the energy of the incoming photon is the difference of energy levels at E_2 and E_1. Emission of a photon will take place if there is a transition from a state with energy E_2 to a state with energy E_1.

A Q-switched laser produces pulses of tens of nanoseconds duration while a mode-locked laser produces repetitive pulses of tens of picoseconds duration. The Q-switch is operated in two steps. Firstly, the rod is excited by flashlamp by artificially maintaining the losses in the resonator high. Secondly, after 200 microseconds, the losses are removed, such that the ions relax at the same time. The resulting light pulse lasts for about 10 nanoseconds while delivering upto 200mJ with the repeatability rate of 100Hz for the CFR200.

Flash lamp power is distributed over a wide wavelength range and is only available in short pulses and all wavelengths are absorbed by Nd:YAG crystal. The maximum output power of a Nd:YAG system using flash lamps as the optical pump source is 2000 watts Davis (2011). Nonlinear crystals in combination with other optics can be used to generate wavelengths other than the fundamental 1064nm. They include 532nm, 355nm, and 266nm, as well as more eye-safe 1574nm radiation. The most efficient wavelength of a Nd:YAG laser is 1064 nm which has been shown to have a quantum efficiency up to 50% The adjustable parameters of lasing system are flash lamp voltage, the higher the voltage the higher the output power of the laser. However the drawback of increased voltage is the reduced lifetime of the lamp. The default value is 570V. The second adjustable parameter is FL-QS delay, it allows the user to adjust time delay between the triggering of the flashlamp and the Q-swtich. The deviation from the optimal value of 180 microseconds will decrease the output energy.

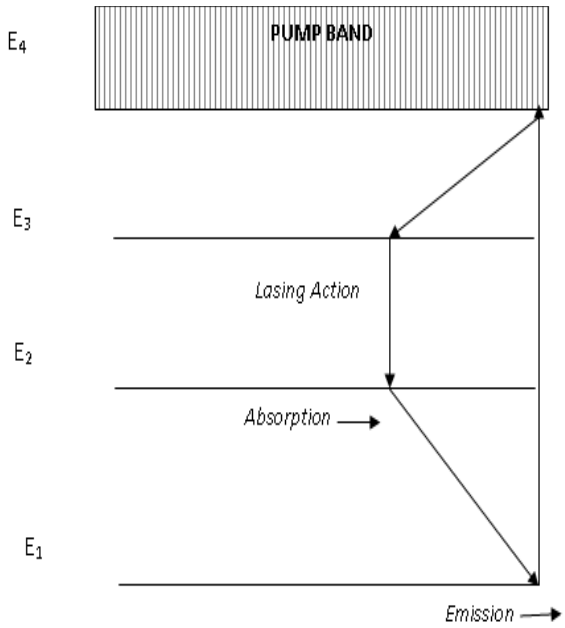

Figure 3: Energy level system of Nd:YAG laser

2.0.3 Image Acquisition

The camera FASTCAM from the firma Photron was used in the current experiments with the spatial resolution of 1024×1024. The camera transferred the data directly to the separated hard drive, which was linked through a port to PC. The camera was synced with the internal frequency of the laser pulse and it recorded 100 frames per second. In all the runs, the recording arrangements were stationary with respect to the tank. The lens used in the camera is Carl Zeis, Makro Planar with focal length F is 50mm and the maximal aperture 2F. Since the light was critical parameter for the current experiments therefore 50mm lens was installed to cover the field of view, which is limited by the laser enlighted planer area. The camera had to be placed such that the optical axis was perpendicular to the light sheet and had to be focused correctly. The camera was centered along the area with maximum light gain from the laser underneath the tank.

It had to be ensured that before each run the tank wall must be cleaned and transparent around the measurement area. Later the tank was seeded with the light reflecting tracer particles of 'Pliolite' having diameter in the range of $800 - 355\mu m$. After the particles settled along the layers so that they should not sink on the bottom, recording was performed. If the delay is longer for recording, the particles can sink on the bottom and can block the light and hence generating dark images. After the recording was done the images were analysed and processed in the software Digiflow.

2.1 DigiFlow

The origins of DigiFlow lie in an earlier system: DigImage, introduced in 1988. This earlier system was first released commercially in 1992, and pioneered many uses of image processing in fluid dynamics. DigiFlow builds on experience with DigImage from the user view point to provide a more powerful, more flexible, but simpler interface. A central feature of DigiFlow is a powerful macro language (dfc) and interpreter. This provides users with a flexible environment to automate and customise processing, as well as proving to be a very useful general computational and plotting tool.

It provides an efficient environment for acquiring and processing a wide range of experimental flows to extract accurate quantitative and qualitative output. It also simplifies the

process of acquiring images of the experiments and extracting results and plotting. Real-time processing can also be done using DigiFlow for particle streaks, synthetic schlieren etc. Time series feature of DigiFlow can be used to extract the intensity image out of the sequence of recorded images. In time series image the data is written to the output image as a row of pixels with each successive time being placed above the previous one.

Digiflow employs a large variety of advance image processing tools and techniques developed for measuring and analysing fluid flows, Digiflow User Guide v3 (2008). Instead of analysing a single image, Digiflow has the designed capabilty of dealing with sequence of images or collection of images in a simple way. DigiFlow uses image selectors to specify image streams for input to and output from a given process. Four types of image streams are supported by it. This includes (i) single image, (ii) movie, which contains multiple images stored in a single file, (iii) sequence in which a collection of related files are used that are identified by a numeric part of the file name that increases by one between neighbouring images in the sequence, (iv) a collection of image files. Input stream can be obtained either by using a feature provided by DigiFlow to capture a a digital video sequence directly from an attached camera supported by DigiFlow, or the recording can be made separately and later the images can be loaded in DigiFlow for processing. For the current set of experiments the processing was done by using movie for paper 2, by recording directly using Digiflow feature, and sequence of images was employed for paper 3 by separately recording and loading afterwards.

Sifting is the process by which images are extracted from in input stream. The extraction process may result in all the images being extracted, or only a subset of images. It provides user with an option to select a subregion of the image i.e. a rectangular window within the image that will be used for processing. It also provides the ability to define, edit and delete coordinate systems providing a mapping between the pixel coordinates of an image and some user-defined coordinate system. In the present study, time series feature of Digiflow was also employed. This feature extracts a one-dimensional array of data from each image in a sequence, and use this to construct an image with one spatial and one temporal dimension. The input streams are normally sequences, while the output streams are individual images. Two such time series images extracted from sequence of images are shown below.

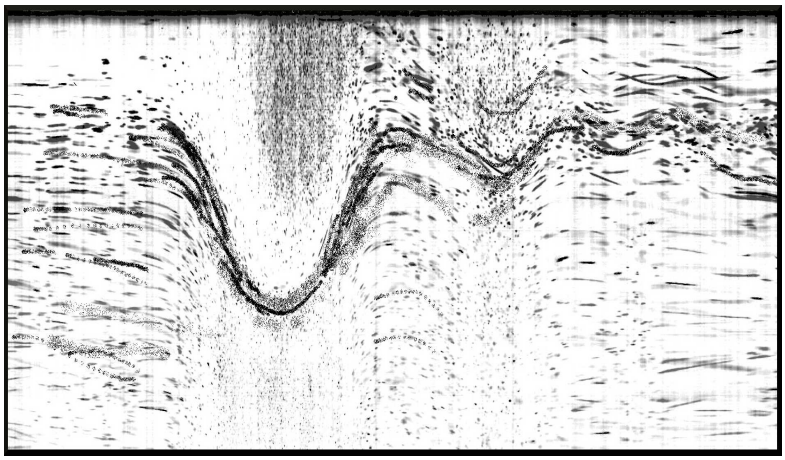

Figure 4: Time series image of the internal wave obtained by Digiflow

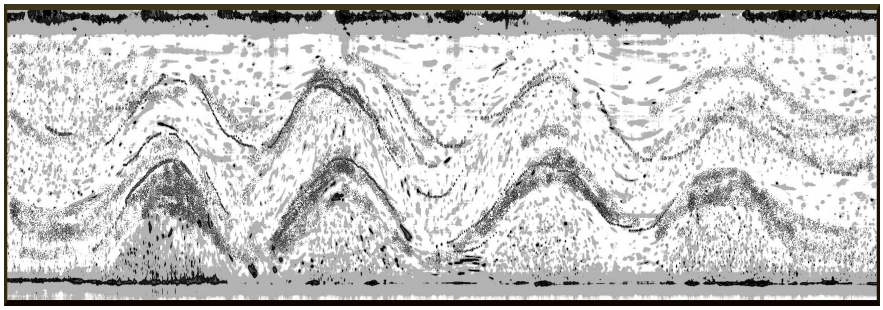

Figure 5: Time series image of the boluses observed at the slope end obtained by Digiflow

Within a variety of tools and features offered by Digiflow for image processing the two main features employed in the current set of experiments are Particle image velocimetery(PIV) and Particle Tracking velocimetry(PTV). Before loading the recorded images in DigiFlow, they were first masked in Matlab. The masked images were later processed in Digiflow. In Digiflow, the standard PIV process takes two input streams. The interval between these two streams should be specified in the Interrogation interval group. The Mask zeros check box causes DigiFlow to ignore all pixels with an identically zero intensity. This feature is designed to allow simple masking of images. Such masking may be used to remove parts of the field of view that do not contain the flow. There are four groups of controls on the Inputs tab. The first controls maximum displacement that will be searched for. The values x Max shift and y Max shift are specified in pixels and are assumed symmetric about zero. These values relate to the maximum expected particle displacement but need to be as large as that shift (they parameterise the initial search space for the particle displacement, but DigiFlow will search a larger space if necessary). The velocity field has a significant bias in one direction of flow, then specifying a nonzero x Bias and/or y Bias will allow greater computational efficiency by permitting smaller values for x Max shift and y Max shift.

To provide a simplified interface to the internal workings of the PIV algorithm, DigiFlow provides a range of predefined settings that have the effect of producing different resolutions and accuracies. Selection of the most appropriate output file format (between .dfd and .dfi) depends on the type of post processing to be undertaken. For the current set of experiments, to run the PIV in digiflow the window size was adjusted to 64 by 64 or 32 by 32 depending on the seeding.

Particle Tracking Velocimetry (PTV) differs from Particle Image Velocimetry (PIV) in a fundamental way. PIV relies on pattern matching in an essentially Eulerian way, and PTV seeks to identify individual particles (or other equivalent features) and follow them in a Lagrangian sense. Particle tracking offers a more fundamental approach to PIV. The two-dimensional particle tracking techniques are utilised by DigiFlow. This method represents an efficient, reliable approach to tracking particles from a two-dimensional projection of a flow. The basic strategy behind the particle location is to scan through the image for blobs that have an intensity satisfying some threshold requirement. The

particle location procedure ultimately records not only the location of the particle (as determined by its volume centroid, relative to the threshold, but also a broad range of other particle characteristics, some of which are used in the subsequent matching process.

The DigiFlow PTV facility takes an input stream, showing the experiment, and produces an output stream that contains the particle locations, particle properties, and the inter-frame particle associations. The Input stream may be in any valid image format. The Output stream should be specified as a .dft file. This special file format contains all the particle data and its associations. The particle tracking process is undertaken in pixel space. However the results will generally be required in world coordinates. In DigiFlow the transformation between the two is made during the analysis stage by selecting the appropriate Coordinate system.

For particle tracking velocimetry, again the images were masked. For PTV the images were masked only from top and bottom the width was unaltered inorder to capture the wave propagation along the slope and appearance of boluses by keeping the backdrop on streaks.

3

References

2004 *User's Manual Ultra CFR ND:YAG Laser System*. Big Sky Laser.

2008 *DigiFlow User Guide*. Dalziel Research Partners (2000-2008), version 3.0.

Apel, J.R., Holbrook, J.R., Liu, A.K. & Tsai, J.J. 1985 The Sulu Sea internal soliton experiment. *J. Phys. Oceanogr.* **15**, 1625–1651.

Cai, S.Q., Long, X.M. & Gan, Z.J. 2003 A method to estimate the forces exerted by internal solitons on cylindrical piles. *J. Ocean Engineering* **30**, 673 – 689.

Davis, E. 2011 ND:YAG Laser Report. *Tech. Rep.*.

Duda, T.F., Lynch, J.F., Irish, J.D., Beardsley., R.C., Ramp, S.R., Chiu, C.S., Tang, T.Y. & Yang, Y.J. 2004 Internal tide and nonlinear internal wave behavior at the continental slope in the northern south China Sea. *IEEE, J. Oceanic Engineering* **29**, 1105–1130.

Farmer, D.M. & Smith, J.D. 1980 Tidal interaction of stratified flow with a sill in Knight Inlet. *Deep-Sea Res.* **27**, 239–254.

Grue, J. 2004 *PIV and Water Waves*, chap. Internal wave fields analysed by imaging velocimetry, pp. 239–278. World Sientific, Singapore.

Grue, J., Jensen, A., Rusås, P. & Sveen, J.K. 1999 Properties of large-amplitude internal waves. *J. Fluid Mech.* **380**, 257–278.

Helfrich, K.R. 1992 Internal solitary wave breaking and run-up on a uniform slope. *J. Fluid Mech.* **243**, 133–154.

Lamb, K.G. 1994 Numerical experiments of internal wave generation by strong tidal flow across a finite amplitude bank edge. *J.Geophysical Res.* **99**, 843–864.

Raffel, M., Willert, C., Wereley, S. & Kompenhans, J. 2007 *Particle Image Velocimetry*, 2nd edn. Springer Berlin / Heidelberg.

Ramp, S.R., Tang, T.Y., Duda, T.F., Lynch, J.F., Liu, A.K., Chiu, C.S., Bahr, F.L., Kim, H.R. & Yang, Y.J. 2004 Internal solitons in the northeastern south China Sea. Part I: sources and deep water propagation. *IEEE, J. Oceanic Engineering* **29**, 1157–1181.

Sveen, J.K. & Cowen, E.A. 2004 *PIV and Water Waves*, chap. Quantitative imaging techniques and their application to wavy flows, pp. 1–49. World Scientific, Singapore.

Umeyama, M. 2008 PIV Techniques for Velocity Fields of Internal Waves over a Slowly Varying Bottom Topography. *J. Waterway, Port, Coastal, and Ocean Engineering* **134**, 286–298.

Wallace, B.C. & Wilkinson, D.L. 1988 Run-up of internal waves on a gentle slope in a two-layered system. *J. Fluid Mech.* **191**, 414–442.